Micro-X-ray Fluorescence Mapping Data Analysis and Interpretation

Lauren P. O'Neil

A dissertation

submitted in partial fulfillment of the

requirements for the degree of

Doctor of Philosophy

University of Washington

2022

Reading Committee:

David Catling, co-Chair

W. Tim Elam, co-Chair

Dan Fu

Program Authorized to Offer Degree:

Earth and Space Sciences

University of Washington

Abstract

Micro-X-ray Fluorescence Mapping Data Analysis and Interpretation

Lauren P. O'Neil

co-Chairs of the Supervisory Committee:
David Catling, Ph.D.
W. Tim Elam, Ph.D.
Department of Earth and Space Sciences

The Planetary instrument for X-ray Lithochemistry (PIXL) is a micro-XRF instrument on NASA's Perseverance rover. XRF has long been used for analyzing geologic materials, but instrumentation is constantly evolving and capabilities have improved (Anzelmo and Lindsay, 1987a). This work outlines several methods and considerations for analysis and interpretation to make the most of available XRF data. We describe an optimized analytical method for quantifying light elements often omitted from XRF analysis based on Compton and Rayleigh scattered peaks the spectrum in Chapter 2, and in Chapter 3 we outline practical guidelines and limitations of the analysis. This method requires that the scattered peaks have a few hundred counts, which is easily attainable on a standard XRF instrument, and slightly more difficult on a micro-XRF instrument, which has a diminished count-rate. If used, however, it can help differentiate between different classes of minerals that are otherwise indistinguishable by XRF, such as carbonates and oxides.

Micro-XRF mapping uses an x-ray beam focused to ~100 microns to collect spectra across a surface to provide spatially resolved element abundances. This information is often used qualitatively in biology and forensics, but in geology there is potential to lose information about the bulk rock when focusing on such a small area (Tian et al., 2014; Zheng et al., 2019). Chapter 4 addresses how to combine groups of small measurements to extract bulk data, particularly when a surface is heterogeneous on a 100-micron scale. We found that with a 100-micron beam, 25 spots were sufficient, though characterization of mineral components is limited by the size of the grains relative to the beam. Chapter 5 examines the effect of smaller scale structures of only a few microns and how they can alter measurements of sulfur. Coatings of only 0.2 nm around sulfate altered measured sulfur up to 13%, and thicker coatings of 2 microns diminished measured sulfur by 85%.

TABLE OF CONTENTS

1 Introduction 1

1.1 Background 1

1.1.1 X-ray Fluorescence 1

1.1.2 XRF spectra 2

1.1.3 Quantification 3

1.1.4 XRF in Planetary Exploration 4

1.1.5 PIXL 5

1.2 Thesis Outline 5

2 Optimized compton fitting and modeling for light element determination in micro-x-ray fluorescence map datasets 8

2.1 Introduction 9

2.2 Methods 11

2.2.1 Experimental Setup 11

2.2.2 Model Description 13

2.3 Spectrum Analysis 14

2.3.1 Background Subtraction 14

2.3.2 Peak Fitting 17

2.4 Results 19

2.4.1 Models 19

2.4.2 Collection Time 20

2.5 Discussion 22

2.6 Conclusions 24

3 Practical guidelines and limitations on using Compton and Rayleigh scattering in x-ray fluorescence spectra for mineral identification 25

3.1 Introduction 26

3.2 Methods 29

3.2.1 Sample Selection 29

3.2.2 Experimental Setup 31

3.2.3 Modeling 32

3.2.4 Data Analysis 32

3.3 Results 33

3.3.1 Scatter Ratios of Minerals 33

3.3.2 Comparison with Modeled Ratios 37

3.4 Discussion 39

3.4.1 Mineral distinguishability 39

3.4.2 Organic Matter in Shales 40

3.5 Conclusion 42

4 Obtaining bulk-rock properties from micro-X-Ray Fluorescence mapping data 44

4.1 Introduction 45

4.2 Experimental 49

4.2.1 Data Collection 49

4.2.2 Data Analysis 50

4.3 Results 50

4.3.1 Complete dataset 50

4.3.2 Minimum Sampling Requirement 55

4.3.3 Trace Elements and Zero Concentration 59

4.4 Discussion 60

4.4.1 Combining Spectra 60
4.4.2 Minimum Sampling 61

4.5 Conclusion 64

5 Effects of matrix structure on x-ray fluorescence (XRF) measurements: Consistency in sulfur quantification 66

5.1 Introduction 67

5.1.1 Role of sulfur on Mars 67
5.1.2 Quantification and element distribution 68

5.2 Methods 70

5.2.1 Sediment Composition 70
5.2.2 Modeled Structures 72
5.2.3 Software: PIQUANT and XMI-MSIM 74
5.2.4 Modeled Instrument parameters 75

5.3 Results 75

5.3.1 Sulfur Quantification 75
5.3.2 Depth and limitations of Monte Carlo 76

5.4 Discussion 77

5.4.1 Real variability in specimens 77
5.4.2 Overall effect of coatings 78
5.4.3 Sulfur distribution 78

5.5 Conclusion 80

6 Conclusion 81

7 References 83

LIST OF FIGURES

Figure 2.1: Experimental Geometry 12

Figure 2.2: SNIP Artifacts Applying the SNIP algorithm as-is often results in one of two artifacts based on selection of the width. The bremsstrahlung background is expected to be smooth, but a width that is too narrow (left) leaves a bump in the background estimation under wider peaks. When subtracted, this results in wider peaks that appear shorter than they actually are, and an accurate ratio of their areas may not be preserved. A width that is too wide flattens the bremsstrahlung (right) and when subtracted leaves a broad peak. In this case the spectrum does not return to zero between fluorescence peaks where expected. 16

Figure 2.3: Refined SNIP Background The background is calculated using SNIP with a narrower width in the middle region and a wider width at higher energies where the peaks are wider (8 to 18 keV). This combination clips the narrow fluorescence peaks and broader scattered peaks with minimal flattening of the continuum. 16

Figure 2.4: Rayleigh Peak Fit The region between the minima on either side of the Rayleigh peak is fitted to a sum of Gaussians. The Kα1, 2, and 3 lines are fit with the Gaussians of the same width and fixed relative position and height based on the fundamental parameters database. The piece of the Compton peak that overlaps this region is modeled with a Gaussian placed at the Compton shift. When this Gaussian sum is subtracted, the baseline left is a smooth, strictly decreasing spectrum with no unexpected bumps or steps. 18

Figure 2.5: Experimental Versus Model Compton/Rayleigh (C/R) Ratios The MSIM model (left panel) underestimates low scattering ratios and overestimates high ratios compared to experimentally measured values. Ideally, model and experimental ratios would correlate 1:1 (dotted line). The ratio for water is predicted almost 30% too high while Mo is 40% too low. The

fundamental parameters model (right panel) predicts consistently low ratios but given the strong linear dependence may be easily adjusted to bring all errors below 30%. The solid line is the best fit between experimental and model data. 19

Figure 2.6: Compton/Rayleigh (C/R) Ratio at Low Collection Times The C/R ratio was calculated from spectra taken at a range of collection times to investigate the effect of low signal strength. At low collection times, the C/R ratio is relatively larger, but the magnitude of the effect depends on the specific material. 21

Figure 2.7: Maximum and minimum collection times. At 2000 seconds (left), the scattering peaks are very clear and rise well above the baseline. At only one second (right) it is very difficult to observe the shape or tails of the scattering peaks. Without a function to fit the Compton peak, the area is summed over the interval where the peak is expected. The low energy cut-off point is uncertain and therefore somewhat arbitrarily determined. At low signal strength, the baseline makes a much larger contribution to the peak area and is controlled by the cut-off point. 22

Figure 3.1: XRF spectra of gypsum and anhydrite. These calcium sulfates are compositionally different only due to water of hydration in gypsum. We see the same fluorescence peaks in each: Ca fluorescence at 3.7 keV and S florescence at 2.3 keV. Fluorescence is stronger in anhydrite because Ca and S are more concentrated, though overall intensity can also be affected by other factors, such as distance and atmosphere. The water in gypsum adds low-Z elements and increases the size of the Compton peak relative to the Rayleigh peak. 29

Figure 3.2: Geometry for experimental setup 31

Figure 3.3: Compton-to-Rayleigh scatter ratios for different collection time. Data was collected for different durations, with a long collection time leading to higher signal-to-noise and smaller uncertainty. Data for 2000-second collection time not shown. 34

Figure 3.4: Statistical uncertainty versus experimentally observed variation. The statistical uncertainty is determined from the counting statistics expected based on the intensity of the peaks. Experimental uncertainty is the standard deviation of repeated measurements. The line represents a 1:1 relationship. 36

Figure 3.5: Uncertainty of the Compton-to-Rayleigh scatter ratio measurement against area of the Rayleigh peak. A horizontal line is shown at 0.15, above which we have observed the measured standard deviation far exceeds the expected statistical uncertainty. Uncertainty crosses into the well-behaved region at roughly 250 counts. 37

Figure 4.1: Granite (left) and diabase (right) samples from the same sites as USGS powdered geochemical reference materials G-1 (granite) and W-1 (diabase). 49

Figure 4.2: Element maps for the granite sample. Data was collected in a 4 mm by 18 mm grid with 100-micron spacing. 13 elements were quantified in each spot, and element distributions are shown. Major, minor, and trace elements are scaled separately. 52

Figure 4.3: Element maps for the diabase sample. Data was collected in a 4 mm by 18 mm grid with 100-micron spacing. 13 elements were quantified in each spot, and element distributions are shown. Major, minor, and trace elements are scaled separately. 53

Figure 4.4: Element concentrations. The concentrations calculated from aggregate spectra formed from the sum of an increasing number of individual spectra. To decrease scatter, each data point shown is the average of 50 aggregate elemental concentrations. Silicon is not shown. Many elements show slight drift (either up or down) when fewer points are summed, as indicated by the arrows. 56

Figure 4.5: Scatter in Measurements. The standard deviation as a fraction of element concentration is plotted against the number of individual spectra included. As expected, when very

few spots are included, there is a lot of variability between sets, while they become less varied when more data is included. The standard deviation decreases faster for higher concentration elements. Silicon is not shown. 57

Figure 4.6: Scatter in measurements of the granite sample. The standard deviation between measurements as a fraction of element concentration plotted against the number of points included. After an initial decrease, the relative standard deviation appears to remain constant over most of this range. Zirconium is omitted from the plot because the concentration is very close to the detection limit and is measured to be zero in much of this data, so the relative standard deviation is not meaningful. 58

Figure 5.1: Simulated configurations. The sulfate layers are 20 μm thick and are spaced such that all the sulfur is removed from the remaining material and the average composition overall is maintained. The sulfur layers are coated with calcium carbonate ($CaCO_3$) in the lake sediment, hematite (Fe_2O_3) in the marine sediment, and salt ((Na, K) Cl) in the Martian soil. When the coatings are added, this material is subtracted from the remaining material to maintain average concentrations. Simulations were done with a coating of thickness 0, 0.2 nm, and 2 μm except for the Martian soil, which was limited to a maximum coating thickness of 0.08 μm by Na and K availability. The thickness of the top layer of coating and remaining material combined was kept constant to minimize the impact of distance on the sulfur quantification. 73

LIST OF TABLES

Table 2.1: Materials. Powder and liquid samples were placed in a cup behind an ultra-thin (3.6 μm) Mylar window. Foil and sheet samples were stacked to the total thickness listed without a window except for the Kapton stack, which was wrapped in Mylar to ease handling. 12

Table 3.1: Mineral specimens. Sets with matching fluorescence signals differ in average atomic number (Z), and therefore have a different scatter ratio. 30

Table 3.2: Modeled Compton-to-Rayleigh scatter ratios. Experimental ratios here are calculated from the longest duration (least noisy) data for each mineral.................................... 38

Table 3.3: Select common components of shales. Limited fluorescence signals combined with a variety of possible feldspar and clay minerals make it impossible to use scatter peaks to learn about organic content of shales. 42

Table 4.1: Composition using the full dataset. The concentrations of 13 elements known to be in both samples are calculated two ways and shown here as weight percent (Fleischer, 1969). First, the individual spectra are summed to form one aggregate spectrum, and this aggregate spectrum is used for quantification. Second, each individual spectrum is analyzed and then the calculated concentrations are averaged. Both methods use the same data; the difference is in analysis only. Error bars are one standard deviation. For major elements such as silicon and aluminum the results differ by only a few percent, but trace elements vary by more, and in many cases, the difference is statistically significant.. 54

Table 5.1: Elemental composition for each matrix in weight percent................................... 71

Table 5.2: Measured sulfur concentrations, in weight percent.... 76

1

INTRODUCTION

1.1 Background

1.1.1 X-ray Fluorescence

Throughout this work, we analyze x-ray fluorescence (XRF) spectra. XRF is based on the fact that atoms emit characteristic energies when subjected to appropriate excitation. Here, we use an x-ray tube to irradiate our samples, though other radioactive sources are also possible. The beam interacts with the sample and produces the measured spectrum, which primarily consists of fluorescence photons. We analyze an energy-dispersive spectrum that covers energies from a few keV up to 40 keV. The lower limit is controlled by absorption in the detector, mainly its beryllium window, while the upper limit is controlled by the voltage generated in the x-ray tube for excitation. At these energies, we are probing the inner K-shell electrons and their transitions. These electrons are not involved in bonding as valence electrons are, so molecular and crystal structure are invisible to this method. Emissions as electrons relax into the K-shell from the M (K-alpha) or L (K-beta) shell generate the strongest fluorescence lines, and in a typical spectrum we see pairs of florescence peaks corresponding to each element. The energy of an electron level is given by

$$E = R\,h\,\frac{Z^2}{n^2}$$

where R is the Rydberg energy, Z is the atomic number, h is Planck's constant, and n is the integer associated with the level. Emission energies correspond to the difference between the two shells of the electronic transition. The probability of a transition dictates the relative strength of each peak produced in an element's XRF spectrum. The overall strength correlates with the abundance of a particular element in a sample. However, other atoms present can interact with and absorb these emissions before they reach the detector. Generally, we take into account all elements present in a sample when analyzing spectra and compensate for expected re-absorption by other atoms. However, these so-called "matrix effects" can cause problems when a sample is not well mixed, as discussed in Chapter 5.

1.1.2 XRF spectra

The collection of XRF spectra cannot filter out photons from other interactions besides fluorescence and therefore includes x-rays from any other interactions within our detectable energy bounds. After fluorescence, scattering is the next largest contributor to the spectrum. There are two varieties of scattering that occur when x-rays scatter off electrons in the specimen: Rayleigh (coherent) and Compton (incoherent). These each produce a copy of the incoming beam, here generated by an x-ray tube, in the measured spectrum, with the Compton scattered photons slightly offset from their initial energy. An x-ray tube spectrum is generated by accelerating electrons into a target anode. The spectrum includes bremsstrahlung radiation from the electrons' deceleration as well as fluorescence emitted by the anode. These are both scattered by the sample. Rayleigh scattering is elastic scattering that results in no change to the energy of the photon. Compton scattering occurs when an electron recoils and the scattered photon decreases in energy. The change in wavelength depends on the angle of the scattered photon and is given by

$$\Delta\lambda = \frac{h}{m_e c}\,(1 - cos\theta)$$

where m_e is the mass of an electron, c is the speed of light, h is the Planck constant, and θ is the scattering angle. While the energy lost in Compton scattering does not depend on the identity of the target element, the probability of scattering and the size of the resulting peak do depend on the element. Scattering and what we can learn from that part of the XRF spectrum is the focus of Chapters 2 and 3.

1.1.3 Quantification

XRF spectrometry became a commercially available technique for elemental analysis in the middle of the 20th century. In the decades since, methods of analysis have evolved along with computing power. Initially, complex calculations taking into account fluorescence and scattering of many elements were impractical, and quantification from XRF intensities relied on comparison to standards with known concentrations of particular elements. This severely limited XRF's flexibility as an analytical tool, as it could be used only for samples that were similar to available standards and arbitrary elements could not be analyzed (Tertian and Claisse, 1982).

When spectrometers improved and the means became available, the fundamental parameters (FP) method was developed. This method analyzes the spectrum based on the theory of x-ray interactions, and so does not require standards. Databases of these fundamental parameters exist and are constantly improving (Elam et al., 2002; Schoonjans et al., 2011). FP is much more flexible because spectra for any combination of elements can be calculated and analyzed, and any element in a sample can be quantified, though improvements in spectrum calculations are ongoing and the method continues to be refined (Elam et al., 2006; Michel-Hart and Elam, 2017).

More recently, Monte Carlo (MC) models have been developed. These can account for yet more variation and an arbitrary number of interactions between emitted electrons and the matrix if given enough time. They are also better able to deal with different sample geometries. FP and MC often assume a homogenous sample, but MC has started to be applied to layers and more complex geometries. This work uses two quantification programs, PIQUANT and XMI-MSIM. PIQUANT is based on fundamental parameters while XMI-MSIM uses Monte Carlo.

1.1.4 XRF in Planetary Exploration

XRF and similar instrumentation has been part of planetary exploration for decades. NASA's Viking landers, the first Mars landers, both carried an XRF instrument used to measure the composition of the regolith at each of the two landing sites (Clark et al., 1977). The Soviet Union sent Venera 13 and 14 with an XRF to characterize Venus (Santos et al., 2021; Surkov et al., 1984). XRF provides quantification of a range of elements and works on a variety of sample types including liquids, powders, and natural surfaces. That XRF is nondestructive and can work on natural surfaces without a need for sample preparation makes it appropriate for robotic missions. Alpha Particle X-ray Spectrometers (APXS) share these characteristics and were carried by several other space craft, including NASA's Pathfinder, Mars Exploration Rovers, and Curiosity Rover as well as ESA's Philae Lander (Boehnhardt et al., 2017; Campbell et al., 2012; Gellert et al., 2006; Rieder et al., 1997).

APXS and XRF both quantify the elemental composition of a sample. XRF is based on irradiating a sample with x-rays to excite electrons and induce x-ray emissions from the sample. The x-ray emissions correspond to the energies of electron transitions and are characteristic of each element.

APXS relies on alpha particles as well as some x-rays to induce x-ray emission in the sample, providing two sets of x-ray emissions: x-ray fluorescence (XRF) and Particle Induced X-ray Emission (PIXE). In addition, backscattered alpha particles may be detected and used for Rutherford Backscattering Spectroscopy (RBS). This provides information on lighter elements whose x-ray emissions are not detected in either XRF or PIXE, but requires additional detectors (Campbell et al., 2009; Rieder et al., 2003; Tertian and Claisse, 1982). An APXS instrument requires an alpha particle source while an XRF often uses an x-ray tube to induce emission. These sources have very different power requirements and result in very different signal strength. Instruments designed for different spacecraft use are optimized for their individual missions based on the technology of the time and performance varies.

1.1.5 PIXL

This work is motivated by the inclusion of the Planetary Instrument for X-ray Lithochemistry (PIXL) on NASA’s Mars 2020 rover. This is a micro-XRF mapping instrument that will collect XRF spectra with a beam focused to 120 microns in diameter (Allwood et al., 2020). Such measurements will be taken in groups as the instrument rasters along either a line or a grid to provide a map of XRF spectra and elemental abundances. This reveals the spatial relationship between elements and allows for characterization of distinct mineral components, both of which contribute to understanding the geology of a rock.

1.2 Thesis Outline

This work builds upon current techniques to maximize our ability to analyze, understand, and interpret data collected by PIXL.

In Chapter 2, we analyze the scattered peaks in an XRF spectrum and establish a method for reliable measurement of the ratio of Compton scatter to Rayleigh scatter produced by a specimen. These are the K lines generated in the x-ray tube that are duplicated in the measured spectrum by scattering in the sample. These peaks are very small compared to fluorescence peaks and are often cast out as irrelevant artifacts. However, their size can provide information about the overall composition. Outer, valence, electrons held loosely by a nucleus are more likely to Compton scatter, while inner, core electron held tightly by the nucleus are more likely to Rayleigh scatter. When measured accurately, the relative size of the scatter peaks characterizes the electron population in a sample and relates to average atomic number.

In Chapter 3, we examined the utility of using the ratio of Compton to Rayleigh scatter to distinguish between minerals. Fluorescence is only detectable above about 1 keV (below 1.2 nm), and elements lighter than sodium (Z=11) have fluorescence beyond this cutoff. Such elements include carbon and oxygen, which are of particular astrobiological interest. Their most measurable impact on the spectrum is on the scattered peaks and revealed by the scatter ratio. Minerals such as gypsum and anhydrate, for example, are both calcium sulfates whose spectra contain fluorescence for calcium and sulfur. The additional water (H_2O) in gypsum is only revealed by a change in the scatter ratio. These lighter elements contribute very few core electrons, and therefore increase the proportion of Compton scatter and the scatter ratio goes up. In this chapter, we set practical guidelines for how much signal strength is required to use the scatter ratio to distinguish minerals with the same fluorescence pattern.

In Chapter 4, we consider fluorescence and bulk element quantification using micro-XRF maps. Micro-XRF maps include numerous measurements of small (~100 micron) spots on a rock. Given that rocks are often not homogenous, a single measurement will not adequately characterize the bulk composition. We mapped two samples, a granite and a diabase, and analyzed the variability between repeated measurements. These two specimens contained minerals of distinct colors (white and black) that allowed for easy visual confirmation of grain size and the distribution of minerals in the rock.

In Chapter 5, we examined the impact of small-scale heterogeneity on sulfur quantification. We looked specifically at the effects of coatings around sulfate grains and the matrix effect. We found that for carbonate and salts, the effect was moderate (up to 14%), and for very dense coatings it can be higher (up to 85%), but these types of coatings are not likely.

Altogether, this work enhances the usefulness of PIXL and helps ensure proper interpretation of micro-XRF measurements in heterogeneous samples. While driven by interest in geologic samples, each chapter is also generally applicable to XRF in other contexts.

2

OPTIMIZED COMPTON FITTING AND MODELING FOR LIGHT ELEMENT DETERMINATION IN MICRO-X-RAY FLUORESCENCE MAP DATASETS

L. P. O'Neil, D. C. Catling, and W. T. Elam

Published in Nuclear Instruments and Methods in Physics Research Section B: Beam Interactions with Materials and Atoms volume 436, pages 173–178. (O'Neil et al., 2018)

Abstract

The Planetary Instrument for X-ray Lithochemistry (PIXL) is an X-ray fluorescence instrument scheduled to fly to Mars on NASA's 2020 rover (Allwood et al., 2015). It will be capable of quantifying elements with atomic number of at least 11 using x-ray fluorescence (XRF), but the detector window blocks fluorescence from lighter elements. Important elements otherwise invisible include carbon, oxygen, and nitrogen, which can make up anions in minerals of scientific interest. X-rays scattered by all elements can be detected, so the ratio of Compton to Rayleigh scatter may be measured and used to infer the presence of elements for which there is no detectable fluorescence. We have refined a fundamental parameters model to predict the Compton/Rayleigh ratio for any given composition that can be compared to an experimentally measured ratio. We compare with a published Monte Carlo model (Schoonjans et al., 2012) and to experimental values for a set of seven materials. Compton/Rayleigh ratios predicted by the model are in good, though imperfect, agreement with experimental measurements. A procedure for consistently computing

the Compton/Rayleigh ratio from a noisy spectrum has also been developed using a variation on a common background removal method and peak fitting.

2.1 Introduction

The Planetary Instrument for X-ray Lithochemistry (PIXL) is intended to fly on NASA's Mars 2020 rover (Williford et al., 2018). The purpose of PIXL is to quantify elemental abundances in Martian rocks and regolith, and it can do this using X-ray fluorescence for elements heavier than sodium. In places where data is limited, such as Mars, it is desirable to analyze both X-ray fluorescence and X-ray scatter that appear in the same spectrum.

Both Compton (incoherent) and Rayleigh (coherent) scattering occur at some level for all elements, but the relative strength of the scattering varies with composition. The cross section for Rayleigh scattering approximately varies with Z^3, where Z is atomic number, while the Compton scattering varies with Z, so the Compton/Rayleigh ratio decreases roughly as Z^{-2} (Manninen et al., 1984; Manninen and Koikkalainen, 1984). Calculated more precisely, this ratio can reveal the presence of otherwise invisible elements. Peaks in the spectrum that arise from the anode in the X-ray source and scatter off the sample provide a signal from which we can measure the Compton and Rayleigh scatter separately. This idea has been used to determine the average atomic number in previous studies (often indicated as Z_{eff}) (Hodoroaba and Rackwitz, 2014).

With a micro-XRF mapping instrument such as PIXL, datasets can be large and include hundreds of spectra. Speed is more of an issue and as collection time decreases, signal-to-noise does as well, so an automated procedure that can handle more noise is necessary. This is done by using the entire area of the Compton and Rayleigh peaks rather than the height as a measure of intensity.

Furthermore, we compare the measured Compton/Rayleigh ratio to a model rather than correlating it to average atomic number to improve both the accuracy, flexibility, and generality of the relation. Commonly, the ratio decreases with atomic number, but there are exceptions. Silicon, for example, has a higher ratio than calcium carbonate even though its atoms are on average heavier. This type of anomaly is predictable, and modeling specific compositions can account for it. To determine an empirical relationship between Compton/Rayleigh ratio and Z, a calibration curve must be measured with the correct geometry and sample conditions (Duvauchelle et al., 1999). Angle, shape of the sample surface, and distance between the X-ray source, sample, and detector all affect the intensity of scattered X-rays. A fundamental parameters model and prediction, once validated, can be easily adjusted for variations in experimental setup, eliminating the need for new calibration measurements. Once the ratio has been determined for a sample and the composition is predicted more precisely, this knowledge can be used to adjust for matrix effects and correct absolute fluorescence intensities, increasing overall accuracy (Nielson, 1977).

Using the analysis presented here, one can infer the presence of elements with $Z<11$ that are otherwise invisible to an XRF instrument like PIXL. Elements such as carbon and oxygen are below this atomic number limit, and these particular elements may improve understanding of Mars' past climate. Past high levels of carbon dioxide in the atmosphere may have ended up as carbonate minerals through geochemical sequestration, and water may have become trapped in hydrated minerals. Similar analysis has been done for the alpha particle X-ray spectrometers

(APXS) carried by previous Mars rovers (Campbell et al., 2013; Perrett et al., 2016). Scattered peaks were successfully used by Curiosity's APXS to identify pure SiO_2 rather than other silicon-containing minerals such as silicates (Squyres et al., 2008). Carbonates, sulfates and perchlorates (and states of hydration of the latter two mineral types) all potentially provide information about Mars' past environment. In turn, the environment sets constraints on past habitability and astrobiology. The blindness to light elements is a common problem that limits the information provided by X-ray fluorescence spectra, and we seek to expand this limit.

2.2 Methods

2.2.1 Experimental Setup

Experimental spectra were measured with the geometry and apertures shown in Figure 2.1. The X-ray source used was a Comet X-ray tube with a silver anode and the spectrum was measured with an Amptek x-123 SDD. Tube voltage and current were 40 kV and 5 μA, respectively. Samples included pure elements as well as water and a polyimide and are summarized in Table 2.1. To validate the fundamental parameters model, spectra were measured eight times for 2000 seconds each. The Compton/Rayleigh ratio was calculated from each and averaged.

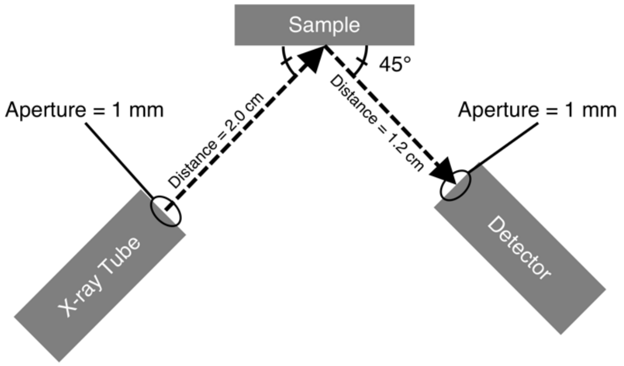

Figure 2.1: Experimental Geometry

Table 2.1: Materials. Powder and liquid samples were placed in a cup behind an ultra-thin (3.6 μm) Mylar window. Foil and sheet samples were stacked to the total thickness listed without a window except for the Kapton stack, which was wrapped in Mylar to ease handling.

Material	**State**	**Thickness (cm)**
Calcium Carbonate	Mallinckrodt calcium carbonate powder, 99.0+%	1.0
Copper	Alfa Aesar copper foil, 0.127mm sheet, 99.99+%	0.0127
Kapton	DuPont 0.003inch sheets	0.4
Molybdenum	Alfa Aesar molybdenum foil, 0.0125mm sheets, 99.95%	0.015
Nickel	Nickel foil, 0.2mm sheets	0.08
Silicon	0.04cm wafers	0.120
Water	Macron HPLC grade water, 6795-10	1.0

Many additional spectra were taken to examine the effects of low signal strength. For these brief collections, 10 measurements were taken of each sample at each time point.

2.2.2 Model Description

Modeling of specific compounds is more precise and versatile than correlating the average atomic number and scattering ratio. In past studies, rather than predicting a ratio for each possible composition, a relationship between average atomic number and scattering ratio has been determined experimentally (Hodoroaba and Rackwitz, 2014; Kurudirek and Büyükyıldız, 2016). However, there is not a strict relationship and modeling can eliminate error. Given that scattering measurements are not the primary purpose of XRF (hence F for fluorescence), signal strength is expected to be sub-optimal and elimination of this error is advantageous. Modeling can also accommodate unforeseen changes in sample geometry and conditions without the need to recreate a calibration curve. Modeled spectra were created from a new fundamental parameters model as well as an independently developed Monte Carlo model, XMI-MSIM (Schoonjans et al., 2012). The models were run to mimic our experimental setup as closely as possible to generate modeled spectra. The same fitting procedure was applied to these modeled spectra as to the measured spectra to generate a modeled ratio for each sample composition.

Sample fluorescence lines calculated by each model are qualitatively indistinguishable, and the main differences are in the scattered peaks. The fundamental parameters model used here calculates primary and secondary fluorescence and fluorescence cascade as given by Tertian and Claisse (Tertian and Claisse, 1982). The tube spectrum is calculated according to Ebel (Ebel, 1999), and Compton and Rayleigh scattering is computed based on theory presented by van Sprang and Bekkers (Sprang and Bekkers, 1998). Constants and data are drawn from a database previously published by Elam et al.(Elam et al., 2002).

2.3 Spectrum Analysis

2.3.1 Background Subtraction

The spectrum of radiation emitted by the X-ray tube includes fluorescence lines from the anode in addition to bremsstrahlung radiation, which forms the continuum. While some X-rays are absorbed, others scatter off the sample and are collected in the measured spectrum. Of interest here are the scattered anode fluorescence lines, which appear as distinct peaks; the scattered bremsstrahlung continuum is background to be subtracted. Each anode fluorescence line produces a Rayleigh scattered peak and a Compton scattered peak that can be used to calculate a Compton/Rayleigh ratio. They sit on top of the scattered continuum, so the continuum must be estimated to calculate the area of the Compton and Rayleigh scattered peaks and their ratio.

A more accurate background estimation is required because scattered peaks are typically an order of magnitude weaker than fluorescence from the sample. Background removal methods that work for standard XRF analysis are insufficient because scattered peaks are small compared to the error in baseline estimation. The shape of the background from the scattered continuum is controlled by the spectrum that is emitted by the tube, absorption, Rayleigh and Compton scatter in the sample, and attenuation in the detector. This combination has placed it beyond our ability to model from first principles with sufficient accuracy for peak fitting, though others have attempted (Hodoroaba et al., 2010). Therefore, we calculate the background continuum empirically from the measured spectrum using a variation on the SNIP algorithm (Van Espen, 2002). Statistical nonlinear iterative peak clipping (SNIP) removes peaks from a spectrum by lowering points that are above the average of their neighbors. The adjustable parameters are the width (how close the neighbors are) and the number of iterations. Increasing iterations flattens the spectrum, and an infinite number would yield a flat line at the lowest point. The SNIP width works most efficiently when tuned to the peak width so that points in the peak are compared to points in the baseline. A width that is too narrow takes many iterations to clip a peak down to baseline, while one that is too wide loses sensitivity to the shape of the background. Sample fluorescence peaks are quite narrow, the scattered peaks are broader, and the bremsstrahlung continuum has a peak that is generally even broader. The ideal algorithm would clip the fluorescence and scattered peaks without substantially altering the peak in the continuum.

Applied without adjustment, the SNIP algorithm either computes a background that fails to completely remove the scatter peaks, or flattens the continuum too much, as demonstrated in Figure 2.2, and sometimes it does both. To avoid this problem and retain accurate peak amplitudes, we select two widths and use them in different zones of the spectrum. The location of the continuum peak is determined by the physical parameters of the X-ray tube and is therefore approximately the same in every spectrum. In that region, a smaller width will diminish the fluorescence peaks much more quickly than the broad continuum peak. In the rest of the spectrum, a slightly wider width is used to remove the scattered tube peaks along with the fluorescence peaks from the specimen. An example is shown in Figure 2.3. There is always some flattening of the continuum, particularly if there are no fluorescence peaks. The most common artifact is a peak at the location of the continuum peak, and simple samples with few fluorescence lines are particularly susceptible.

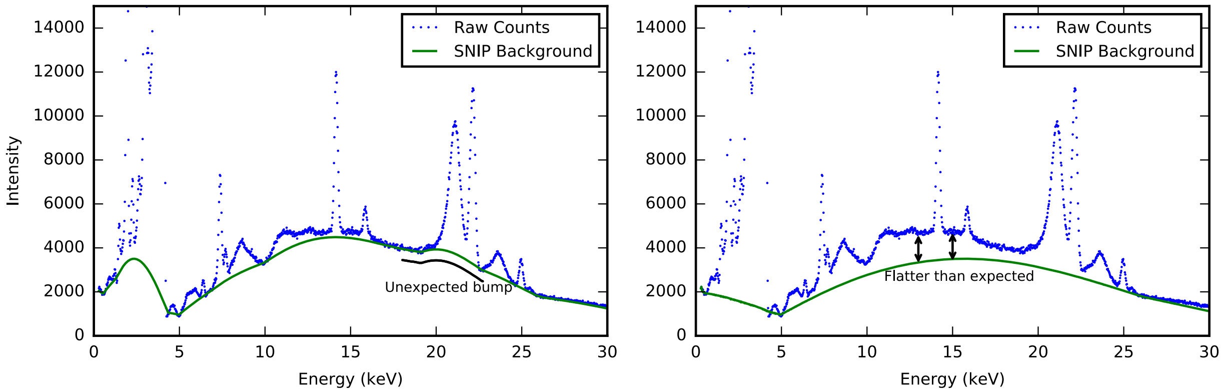

Figure 2.2: SNIP Artifacts Applying the SNIP algorithm as-is often results in one of two artifacts based on selection of the width. The bremsstrahlung background is expected to be smooth, but a width that is too narrow (left) leaves a bump in the background estimation under wider peaks. When subtracted, this results in wider peaks that appear shorter than they actually are, and an accurate ratio of their areas may not be preserved. A width that is too wide flattens the bremsstrahlung (right) and when subtracted leaves a broad peak. In this case the spectrum does not return to zero between fluorescence peaks where expected.

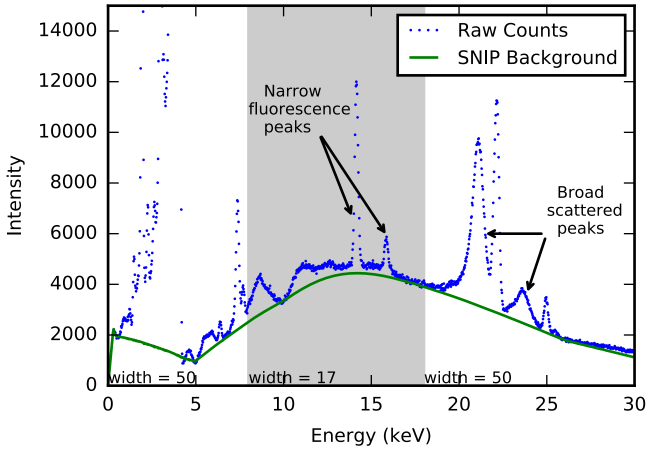

Figure 2.3: Refined SNIP Background The background is calculated using SNIP with a narrower width in the middle region and a wider width at higher energies where the peaks are wider (8 to 18 keV). This combination clips the narrow fluorescence peaks and broader scattered peaks with minimal flattening of the continuum.

Other methods considered were a polynomial fit (van Espen et al., 1977) and cubic splines (Yi et al., 2015). The polynomial fit required a 12-degree polynomial to fit qualitatively well and consistently underestimated the baseline below the scattering peaks. It also changed substantially in reaction to small variations in the spectrum and so yielded inconsistent results. The cubic spline method did not work well with overlapping peaks, which are quite common even in simple samples, and so was unusable.

2.3.2 Peak Fitting

To determine the ratio of Compton to Rayleigh scattering, the area of the scattered silver Kα line is used because this is the strongest of the scattered peaks. We use Gaussians to fit the Rayleigh peak and rely on numerical integration for the Compton peak.

The area of the Rayleigh peak is calculated from a fitted curve. The function is a sum of Gaussians for each of the Kα1, Kα2, and Kα3 lines. The relative energies, widths, and intensities are fixed using the fundamental parameters database. The Kα3 contribution is tiny and does not make a noticeable difference, but it is included for completeness. The region under the Rayleigh peak is fit with this sum and the tail of a Gaussian to stand in for the overlap of the Compton peak. The Compton Gaussian is fixed at the expected energy, but intensity and width are adjusted during the fit. This approximation fits well and when the Rayleigh peak is subtracted leaves a smooth spectrum with no obvious inaccuracies, as shown in Figure 2.4.

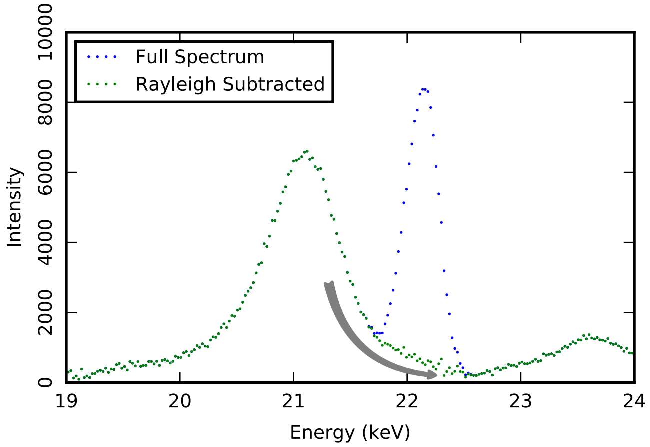

Figure 2.4: Rayleigh Peak Fit The region between the minima on either side of the Rayleigh peak is fitted to a sum of Gaussians. The Kα1, 2, and 3 lines are fit with the Gaussians of the same width and fixed relative position and height based on the fundamental parameters database. The piece of the Compton peak that overlaps this region is modeled with a Gaussian placed at the Compton shift. When this Gaussian sum is subtracted, the baseline left is a smooth, strictly decreasing spectrum with no unexpected bumps or steps.

The area of the Compton peak is determined by numerically integrating the spectrum over both peaks and then subtracting the area of the Rayleigh peak as determined by the fit. We have been unable to find a functional approximation of the Compton peak shape that yields consistent results. The Compton peak has asymmetrical tails whose contributions vary with sample composition, and attempts to fit it have led to either qualitatively poor fits or require too many free parameters to be useful (Van Gysel et al., 2003). The numerical integration employed here can lead to problems with the baseline estimation and the low energy tail of the Compton peak. If the baseline estimation drifts too high or too low across this region, all the extra or missing area is attributed to the Compton peak rather than splitting it with the Rayleigh peak. The Compton peak is asymmetrical and the extent of the tail on the low energy side is difficult to determine; it can include a non-negligible fraction of the area, and it is increasingly difficult to identify a cutoff energy when the peaks are small relative to the noise. However, if the Rayleigh peak is subtracted well, this procedure yields better results than a simple Gaussian fit and is far more robust than using peak height alone.

2.4 Results

2.4.1 Models

The XMI-MSIM model is based on a Monte Carlo approach, and we find that it underestimates the scattering ratio at lower Z values and overestimates it at higher values, as shown in Figure 2.5. It may be possible to further improve its predictive power by adding a correction factor to account for this mass dependent drift.

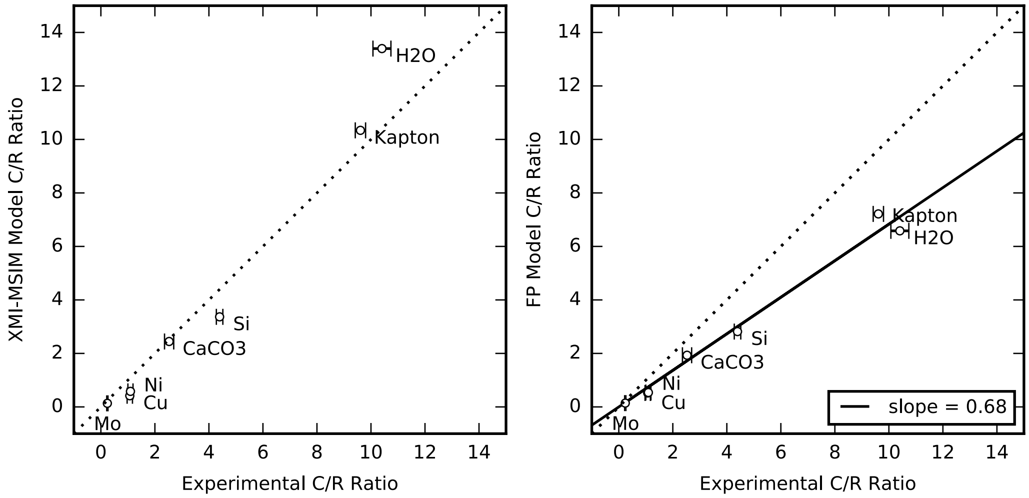

Figure 2.5: Experimental Versus Model Compton/Rayleigh (C/R) Ratios The MSIM model (left panel) underestimates low scattering ratios and overestimates high ratios compared to experimentally measured values. Ideally, model and experimental ratios would correlate 1:1 (dotted line). The ratio for water is predicted almost 30% too high while Mo is 40% too low. The fundamental parameters model (right panel) predicts consistently low ratios but given the strong linear dependence may be easily adjusted to bring all errors below 30%. The solid line is the best fit between experimental and model data.

The fundamental parameters (FP) model consistently underestimates the C/R ratio for all samples, but the correlation is strong. The FP model predictions can be made to match experiment with very little scatter with a simple correction factor of 0.68. Here, our approach is empirical: we wish to determine a predictive relationship that works. An attempt to understand mismatches between the FP model, XMI-MSIM model, and the experimental results would be interesting but is beyond the scope of this paper.

2.4.2 Collection Time

Our fitting approach uses the area of the scatter peaks to take advantage of all photons under both scatter peaks, which considerably reduces fluctuations from counting statistics compared to just using peak height. Such improvement is important for the PIXL spectrometer since data volume and operations on Mars will limit data collection time. This motivated us to study the performance of our approach for extremely short collection times.

Ratios calculated from spectra with low collections times are often higher than those calculated from spectra with long collection times for the same material. Shown in Figure 2.6, the measurement may become significantly inaccurate when the collection time is less than about one minute. This is likely due to SNIP underestimating the baseline in this region. This would add area to the Compton peak and raise the ratio.

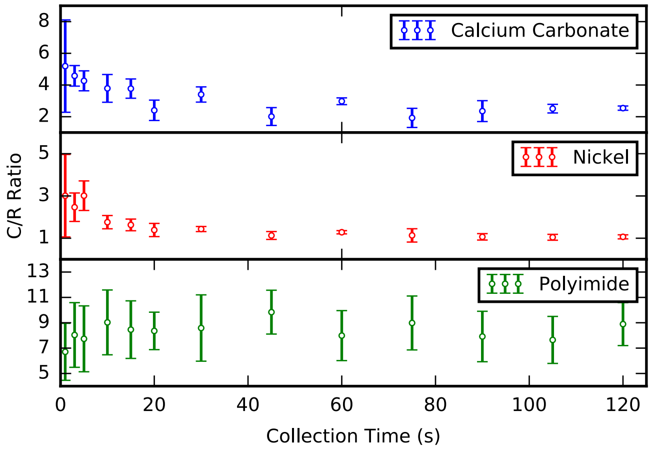

Figure 2.6: Compton/Rayleigh (C/R) Ratio at Low Collection Times The C/R ratio was calculated from spectra taken at a range of collection times to investigate the effect of low signal strength. At low collection times, the C/R ratio is relatively larger, but the magnitude of the effect depends on the specific material.

When the signal is strong enough, the added area is not significant, but it becomes so when the signal is weak, and as shown in Figure 2.7, it becomes progressively more difficult to determine the effective edge of the peak. The precision of the measurement is also substantially worse at low collection times, as expected. The error does not appear equally in all samples, and the polyimide (Kapton) does not show the same trend, possibly because the total scattering is substantially stronger in this lighter sample. With less absorption, there is still substantial signal even at low collection times. As previously noted, the Compton peak does not conform to the same Gaussian as the Rayleigh or fluorescence peaks in the spectrum, and imposing an ill-fitting curve worsens this low signal trend toward high ratios.

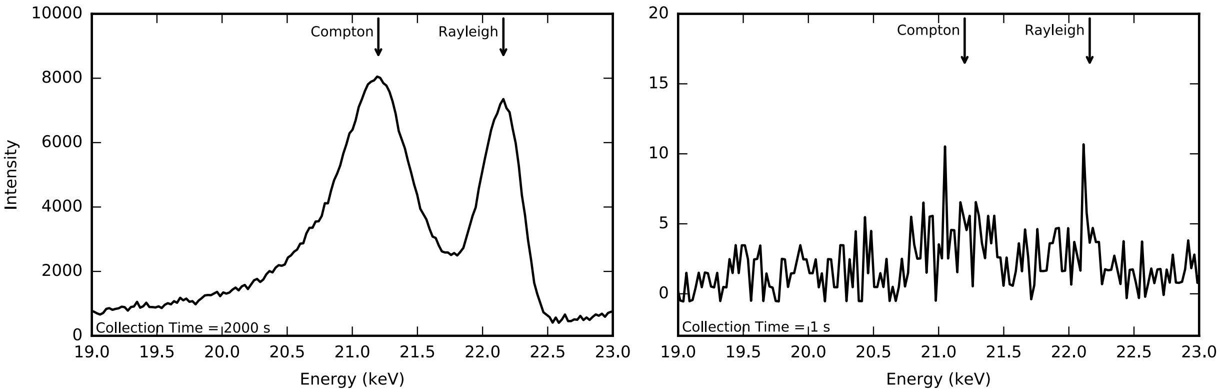

Figure 2.7: Maximum and minimum collection times. At 2000 seconds (left), the scattering peaks are very clear and rise well above the baseline. At only one second (right) it is very difficult to observe the shape or tails of the scattering peaks. Without a function to fit the Compton peak, the area is summed over the interval where the peak is expected. The low energy cut-off point is uncertain and therefore somewhat arbitrarily determined. At low signal strength, the baseline makes a much larger contribution to the peak area and is controlled by the cut-off point.

2.5 Discussion

The proposed analysis of X-ray scattering can supplement X-ray fluorescence data and so provide more deduction of mineralogy. It is optimized for use with noisy data and short collection times to accommodate increased data volumes. It uses a fundamental parameters model to calculate the Compton/Rayleigh ratio directly without an intermediate use of effective atomic number, allowing investigation of diverse light elements in candidate minerals. The calculated ratios are consistently low when compared to experiment but show good correlation. Alone, the scattering ratio is uninformative given that it is not unique; many materials will have the same ratio, so fluorescence data and geologic context of a sample are necessary to guide modeling choices, and then the scattering ratio may be used to narrow down the matching possibilities, ideally to one option. For example, if calcium fluorescence is detected in a rock that may be either calcite ($CaCO_3$) or calcium hydroxide (Ca $(OH)_2$), the ratio for these two possibilities can be predicted via the model and compared to the measured value to identify the sample. We find that fundamental parameters model provides smaller errors than XMI-MSIM, and we are hopeful that further measurement of more complex mineral samples will support its accuracy.

The plausibility of using this strategy on real data will depend on the signal strength (dependent on collection time), accuracy of the model, and composition of the sample. Longer collection times yield more accurate results, and the skew toward higher scattering ratios at low collection times is concerning. Scanning micro-XRF instruments such as PIXL take many spectra in a grid to form a map, and while single spectra taken by PIXL will almost certainly not have the strength to yield conclusive results, by summing similar spectra associated with the same mineral, it may be possible to generate a strong enough signal. The accuracy of the model in geologically relevant minerals has yet to be determined, but further study will quantify the error and precision. Samples with lighter cations are more easily distinguished by the scattering ratio because a change in hydration state or anion represents a larger percent change in average Z, which leads to a proportionally larger change in the scattering ratio. Calcium compounds, for example, will be more easily identified than iron oxides, which have only slight differences in scattering ratio and may well be indistinguishable.

The presence and history of water on Mars is crucial to understanding the planet's past habitability, and light elements to help identify specific mineral phases could prove crucial. The hydration state of compounds in minerals presently on the surface is therefore particularly interesting. The Mars 2020 rover has only two instruments capable of observing the surface at fine resolution

(SHERLOC and PIXL), and neither can nominally quantify the light element content. However, using a modified SNIP background and calculating the ratio of Compton to Rayleigh scattering as outlined here is at present the simplest technique to obtain high resolution mineral data.

2.6 Conclusions

Here we present a methodology to take full advantage of scattered x-ray peaks in XRF spectra taken at short collection times, as in micro-XRF maps. The calculation of the bremsstrahlung baseline and intensity of the scattered peak area is improved for a more robust result. The fundamental parameters model provides a way to distinguish compounds with more certainty than effective atomic number alone. This makes the Compton/Rayleigh ratio a usable measurement in more contexts to determine a more complete composition of a target material.

Acknowledgements

This work was supported by the National Aeronautics and Space Administration as part of the Mars 2020 Project. The support was provided via subcontract 1542830 from NASA's Jet Propulsion Laboratory.

3

PRACTICAL GUIDELINES AND LIMITATIONS ON USING COMPTON AND RAYLEIGH SCATTERING IN X-RAY FLUORESCENCE SPECTRA FOR MINERAL IDENTIFICATION

L. P. O'Neil, W. T. Elam, and D. C. Catling

Abstract

Compton and Rayleigh scatter peaks reveal the presence of light elements not otherwise detectable in an XRF spectrum, but they are relatively small peaks compared to fluorescence. Here, we examine the practical utility of these peaks in distinguishing minerals. Sets of minerals were selected that have the same fluorescence signal but different light elements: gypsum ($CaSO_4 \cdot 2H_2O$) and anhydrite ($CaSO_4$), calcite ($CaCO_3$) and monohydrocalcite ($CaCO_3 \cdot H_2O$), magnesite ($MgCO_3$) and hydromagnesite ($Mg_5(CO_3)_4(OH)_2 \cdot 4H_2O$), epsomite ($MgSO_4 \cdot 7H_2O$) and hexahydrite ($MgSO_4 \cdot 6H_2O$), azurite ($Cu_3(CO_3)_2(OH)_2$) and malachite ($Cu_2CO_3(OH)_2$), and siderite ($FeCO_3$), magnetite ($Fe_2O_4$), and hematite ($Fe_2O_3$). Different types of minerals are easier to discern. For example, calcium carbonates have more substantially different scatter ratios than magnesium carbonates because calcium is heavier than magnesium, so bound water has a larger effect on the average weight. Additionally, heavier atoms absorb more photons, leaving a weaker scattering signal and increased relative uncertainty. Measurements of these minerals were taken with various collection times to examine the signal strength required for the scattering signal to be useful. We found that 200-300 counts in the Rayleigh peak are required for accurate statistical analysis. The conversion of signal to collection time depends on a variety of other factors, such as

instrument geometry, but can be easily determined for any experimental conditions. Because hydrous and anhydrous mineral forma are similar, we found that calculating expected scatter ratios does not provide sufficient accuracy to make a confident identification, and measuring a standard is recommended.

3.1 Introduction

Micro-X-ray Fluorescence (XRF) is a powerful method for determining elemental abundances but is limited by an inability to detect fluorescence from lighter elements, typically below sodium, which has an atomic number (Z) of 11. The essence of XRF is to use the intensity of fluorescence x-rays to determine the abundance of the elements associated with each set of fluorescence peaks. Lighter elements fluoresce at lower energies which are too low for the detector, and therefore their fluorescence is undetected. The energy of Compton and Rayleigh scattering is based on the energy of incoming x-rays and the geometry of the setup, so the scattering from all elements is at the same energy and can be detected. Scattered x-rays produce a background continuum in the spectrum, but the spectrum produced by an x-ray tube contains peaks associated with the anode, and these peaks are scattered by the sample and provide a clear means of analysis. The ratio of Compton to Rayleigh scatter can be measured and used to constrain the presence of otherwise hidden light elements. However, scattering does not produce separate peaks for each element, so a non-unique ratio is measured and used to complement the fluorescence data. The scatter ratio can be used to detect changes in a surface. If light elements are present in a dust layer or a surface has taken up moisture, the scatter ratio would change to reflect this, but here, we have focused on geologic samples and bulk composition.

NASA’s Mars 2020 rover, Perseverance, carries a micro-XRF instrument, the Planetary Instrument for X-ray Lithochemistry (PIXL). In this data-limited context, there may not be data from other instruments for all samples analyzed by PIXL. Scattered signals are substantially weaker than fluorescence, so it is not always practical to use the scattered data. Signal can be increased by dedicating more time to the measurement. The strength of the scattered peaks is further controlled by the composition of the sample, because some elements absorb and fluoresce more strongly than others. Here, we have selected a suite of minerals to closely examine the practicality of using the scatter ratio for light element determination in astrobiologically relevant materials.

Mineralogy can reveal the environmental conditions under which presently existing rocks formed. Of particular interest are the habitability of these conditions: the history of liquid water, water vapor, and atmospheric density and composition. The search for life is a major part of Mars exploration, and investigation of Mars’ past habitability in a key part. Carbonates and sulfates have both been detected on Mars by NASA’s Curiosity rover in Gale crater as well as by Spirit in Gusev Crater (Ming et al., 2014; Morris et al., 2010). Sulfate minerals may be particularly important in recording past redox conditions (Dehouck et al., 2016; Vaniman et al., 2004).

Many relevant minerals may be found in mudstones and shales or other sedimentary formations. These are particularly good at preserving organic matter, so using scatter ratio to detect organics in shales is particularly appealing. Detection of microfossils is an appealing goal, if difficult and unlikely (Westall et al., 2015). They could not be characterized by PIXL, but would be flagged for further study with another instrument, such as SuperCam or SHERLOC (dos Santos et al., 2016).

In other, more basaltic rocks, the ratio of silicon to oxygen can shed light on silicon content and so volcanic processes and crustal formation or hydrothermal activity (Bandfield, 2002; Morris et al., 2016; Squyres et al., 2008).

Because the scatter ratio is not unique, it is necessary to model the scatter ratios for possible compositions. For example, a measurement showing fluorescence for iron could be metallic iron, iron carbonate, or any of various iron oxides because neither carbon nor oxygen fluorescence is detectable. Geologic context is useful in determining plausible possibilities for a spectrum. The scatter ratio is dependent on not only sample composition, but also experimental conditions, such as scattering angle. Scatter ratios should be recalculated for different instrumental setups and are not universal.

Several models are available to simulate XRF spectra and can been used to calculate the scatter ratio, but ratios can also be measured experimentally. Here we use PIQUANT, software developed specifically for PIXL to calculate each ratio. This approach is flexible in that it allows ratios to be easily recalculated if conditions change. For example, if measurements are made with different atmospheric conditions or at different distances from the sample due to experimental complications, ratios can be recalculated quickly. An alternate approach is to build a calibration curve based on measurement of known samples, as has been done traditionally (Hodoroaba and Rackwitz, 2014; Kunzendorf, 1972). It is possible that this would be more accurate for a narrow range of sample compositions because no approximations would need to be made and all experimental conditions would be automatically accounted for. However, it can be difficult to build a calibration curve for a wide range of samples because while the scatter ratio generally decreases with atomic number, it is not a strict correlation and there are exceptions (Hodoroaba and Rackwitz, 2014; Mikhailov et al., 2019).

3.2 Methods

3.2.1 Sample Selection

The minerals selected are listed in Table 3.1. Those with the same fluorescence are distinguishable only by the scattered peaks and the Compton/Rayleigh ratio, as shown in Figure 3.1. Samples were selected to be geologically relevant and stable enough to be handled and measured.

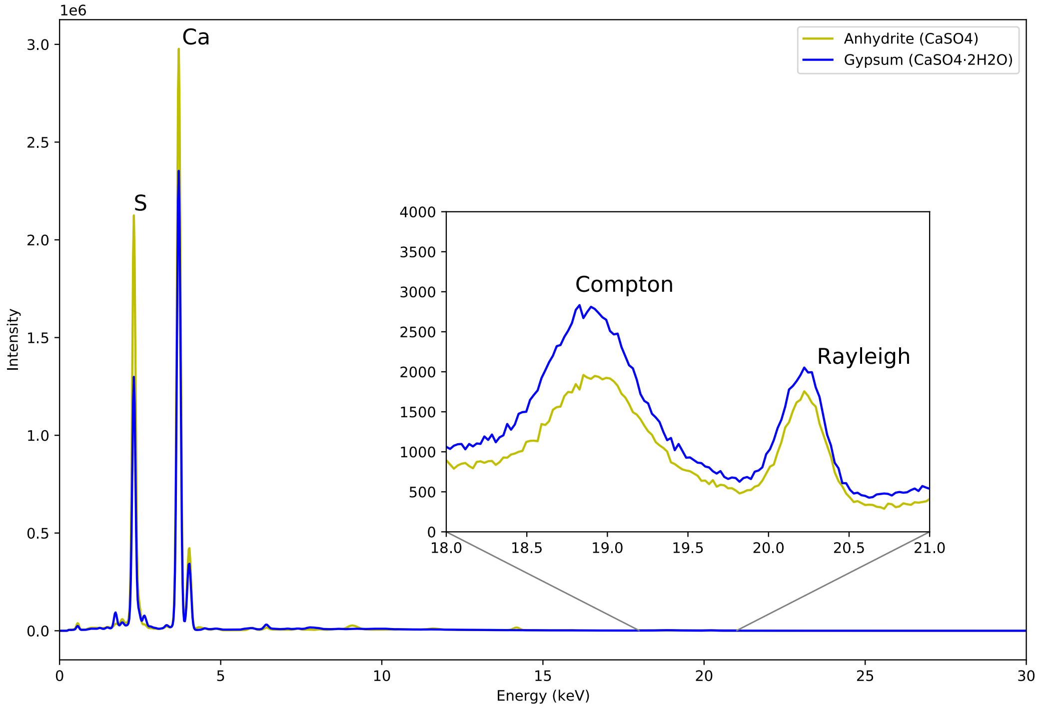

Figure 3.1: XRF spectra of gypsum and anhydrite. These calcium sulfates are compositionally different only due to water of hydration in gypsum. We see the same fluorescence peaks in each: Ca fluorescence at 3.7 keV and S florescence at 2.3 keV. Fluorescence is stronger in anhydrite because Ca and S are more concentrated, though overall

intensity can also be affected by other factors, such as distance and atmosphere. The water in gypsum adds low-Z elements and increases the size of the Compton peak relative to the Rayleigh peak.

Table 3.1: Mineral specimens. Sets with matching fluorescence signals differ in average atomic number (Z), and therefore have a different scatter ratio.

Mineral	Formula	Elements with detectable fluorescence	Average Z
Azurite	$Cu_3(CO_3)_2(OH)_2$	Cu	11.00
Malachite	$Cu_2CO_3(OH)_2$	Cu	10.60
Calcite	$CaCO_3$	Ca	10.00
Monohydrocalcite	$CaCO_3 \cdot H_2O$	Ca	7.50
Anhydrite	$CaSO_4$	Ca, S	11.33
Gypsum	$CaSO_4 \cdot 2H_2O$	Ca, S	7.33
Hematite	Fe_2O_3	Fe	15.20
Magnetite	Fe_2O_4	Fe	14.00
Siderite	$FeCO_3$	Fe	11.20
Hydromagnesite	$Mg_5(CO_3)_4(OH)_2 \cdot 4H_2O$	Mg	6.43
Magnesite	$MgCO_3$	Mg	8.40
Epsomite	$MgSO_4 \cdot 7H_2O$	Mg, S	4.81
Hexahydrite	$MgSO_4 \cdot 6H_2O$	Mg, S	5.00

3.2.2 Experimental Setup

Spectra were collected using an Amptek X-123SDD and a Moxtek transmission-anode x-ray tube with a rhodium anode. Tube voltage and current were 40 kV and 50 μA, respectively. A polycapillary optic focused the beam to an analytical spot size with a 100-micron diameter. The experimental setup was configured with the geometry shown in **Figure 3.2**. Samples were gently filed to expose a fresh, even surface and measured without further preparation in a helium atmosphere. Data were collected for a range of durations to examine trends with signal strength. Durations used (in seconds) were: 2000, 120, 105, 90, 75, 60, 45, 30, 20, 15, 10, 5, 3, and 1. Each sample was measured for each duration nine times: three times at each of three locations as a check on heterogeneities in the sample.

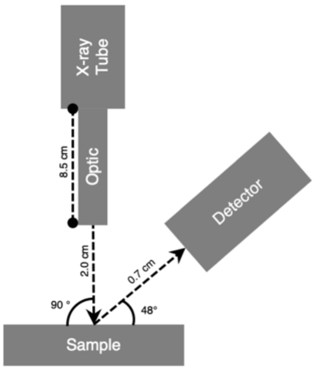

Figure 3.2: Geometry for experimental setup

Iron fluorescence is very nearly one-third of the energy of the Compton peak, and under the conditions described there was potential for pileup to overlap the Compton peak of interest. The Compton peak is analyzed empirically rather than fit to a curve, so such overlap would not be separable or obviously present. Additionally, iron fluorescence is particularly strong, so is more likely to produce pileup than many of the other elements analyzed. Therefore, the settings were adjusted for the iron minerals: hematite, magnetite, and siderite. The tube current was halved, to 25 μA, and all collection times were doubled. This should produce a spectrum with identical fluorescence and scattered peaks, but less pileup. For clarity, iron data are plotted at the equivalent, shorter collection times used for the rest of the minerals.

3.2.3 Modeling

Model spectra for all minerals were generated using PIQUANT version 3.2.6. This x-ray analysis software developed for the Planetary Instrument for X-ray Lithochemistry (PIXL) is a fundamental parameters model. It is based on fluorescence calculations from Tertian and Claisse, x-ray tube calculations from Ebel, scattering calculations from van Sprang and Bekkers and constants and data are from a database previously published by Elam (Ebel, 1999; Elam et al., 2002; Sprang and Bekkers, 1998; Tertian and Claisse, 1982).

3.2.4 Data Analysis

For each spectrum, the ratio of Compton to Rayleigh scattering was calculated. To do so, only the area of the rhodium Kα line was used to measure scattering, as it provides the strongest signal. The continuous bremsstrahlung background was removed using an adjusted-SNIP algorithm, and the scatter ratio was calculated using a combination of Gaussian fits and simple integration according to methodology previously published (O′Neil et al., 2018).

Effort was made to obtain pure minerals, but impurities were inevitable in some cases. The abundance of impurities was quantified using PIQUANT on the longest duration, least noisy spectra for each sample. In most cases, impurities were less than a few percent and therefore have a negligible effect on the scatter ratio. Hematite and magnetite samples contained substantial amounts of Si, and the composition used for modeling has been adjusted to account for it. Additionally, many of the minerals contained crystals that diffracted the x-ray beam, an issue common with micro-focus instruments. Spectra containing diffraction peaks that interfered with the fluorescence or scatter peaks of interest were discarded and recollected at a more suitable point on the sample.

3.3 Results

3.3.1 Scatter Ratios of Minerals

Scatter ratios (Compton/Rayleigh) were calculated for each mineral and are plotted in Figure 3.3. As expected, there is more overlap of error bars at low collection time, and minerals with more substantially different average Z (and scatter ratio) are more easily distinguished than minerals with only slight differences. The error bars here are determined from the standard deviation of repeated measurements. However, we are also interested in whether a mineral can be identified from a single measurement when time or other resource limitations preclude repetition.

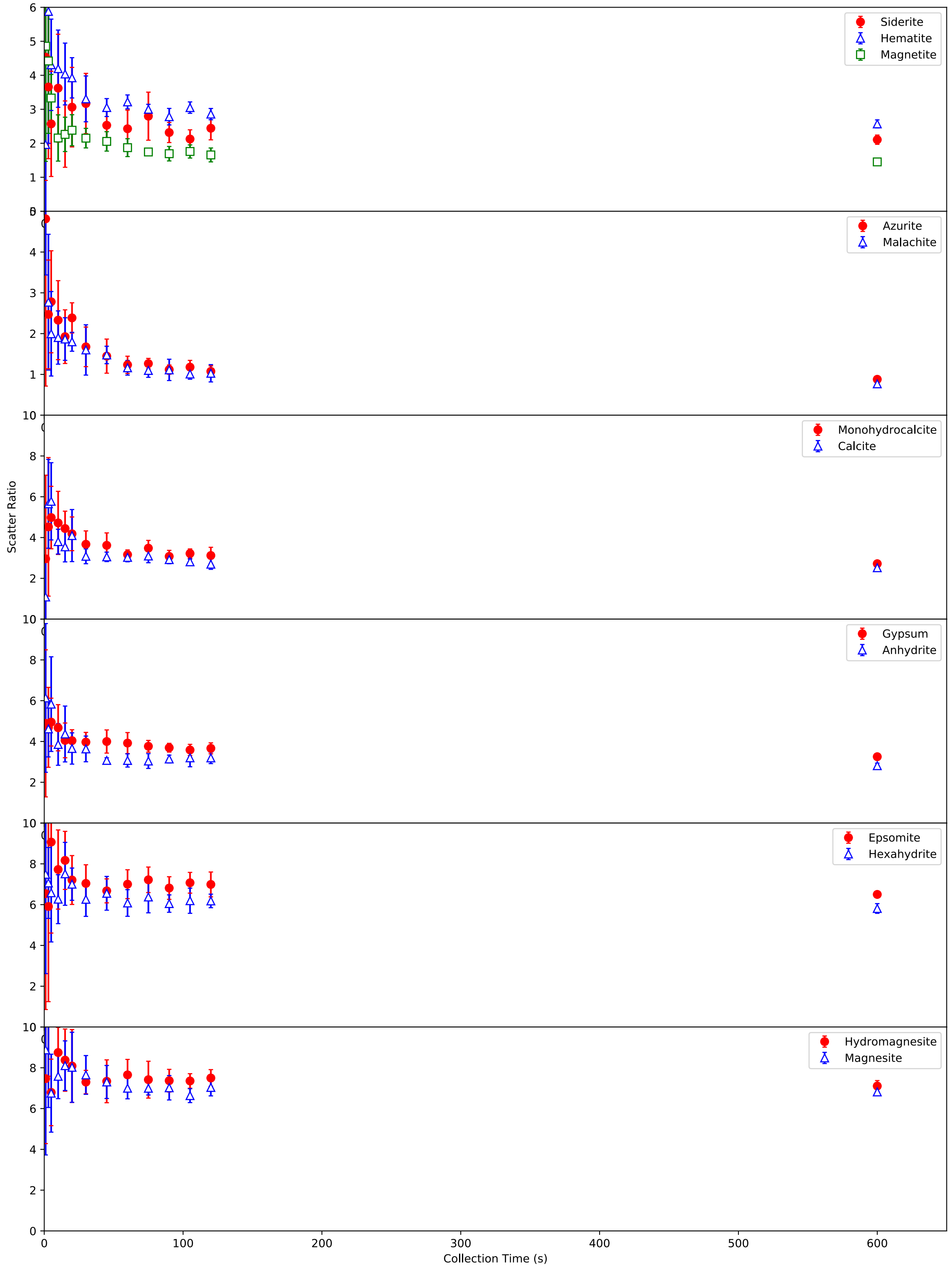

Figure 3.3: Compton-to-Rayleigh scatter ratios for different collection time. Data was collected for different durations, with a long collection time leading to higher signal-to-noise and smaller uncertainty. Data for 2000-second collection time not shown.

On a single measurement, uncertainty can be calculated assuming a Poisson distribution for intensities, as is standard in counting statistics (Bevington and Robinson, 2003; van Grieken and Markowicz, 2002). If our analysis is working well, this statistical uncertainty will match the experimentally observed variation. From our data, we can calculate an experimental uncertainty from the standard deviation, and a statistical uncertainty from the counts on an individual measurement. These are plotted in Figure 3.4. When uncertainty is low, the experimentally measured variation is close to those we expect from counting statistics. However, when the statistical uncertainty of counts is high, particularly above 0.15, the observed variation is much larger. This indicates that when the signal strength is very low, either the counts do not reflect a Poisson distribution, our analytical methods for peak fitting are introducing uncertainty, or there is some other source of experimental error.

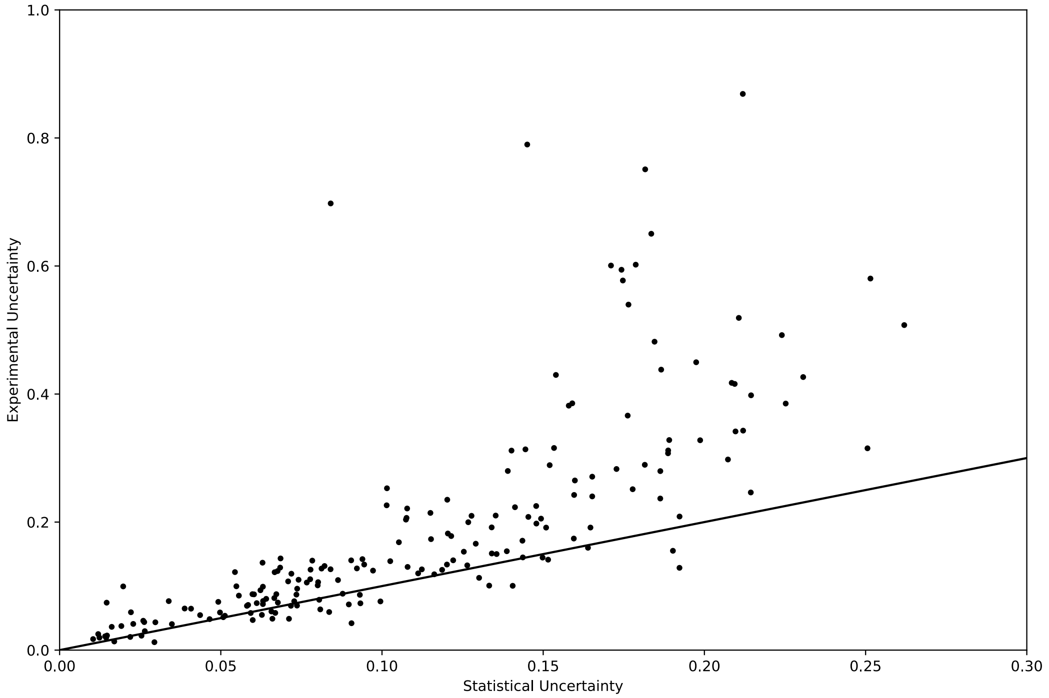

Figure 3.4: Statistical uncertainty versus experimentally observed variation. The statistical uncertainty is determined from the counting statistics expected based on the intensity of the peaks. Experimental uncertainty is the standard deviation of repeated measurements. The line represents a 1:1 relationship.

In practice, it would be useful to know what collection time is required to achieve 15% error or less. Collection time required for a given uncertainty requires a particular signal strength, which is highly dependent on experimental conditions and instrumental setup. Here we examine the area of the Rayleigh peak as a proxy for signal strength. The Rayleigh peak has a well-understood line shape that is easy to analyze, and its area is directly correlated with collection time. By contrast, the Compton line shape is not well characterized and is difficult to consistently analyze. It is straightforward to determine the required collection time from Rayleigh area on a particular instrument. The uncertainty is plotted against Rayleigh area in Figure 3.5, which shows that more than ~250 counts reduces the uncertainty.

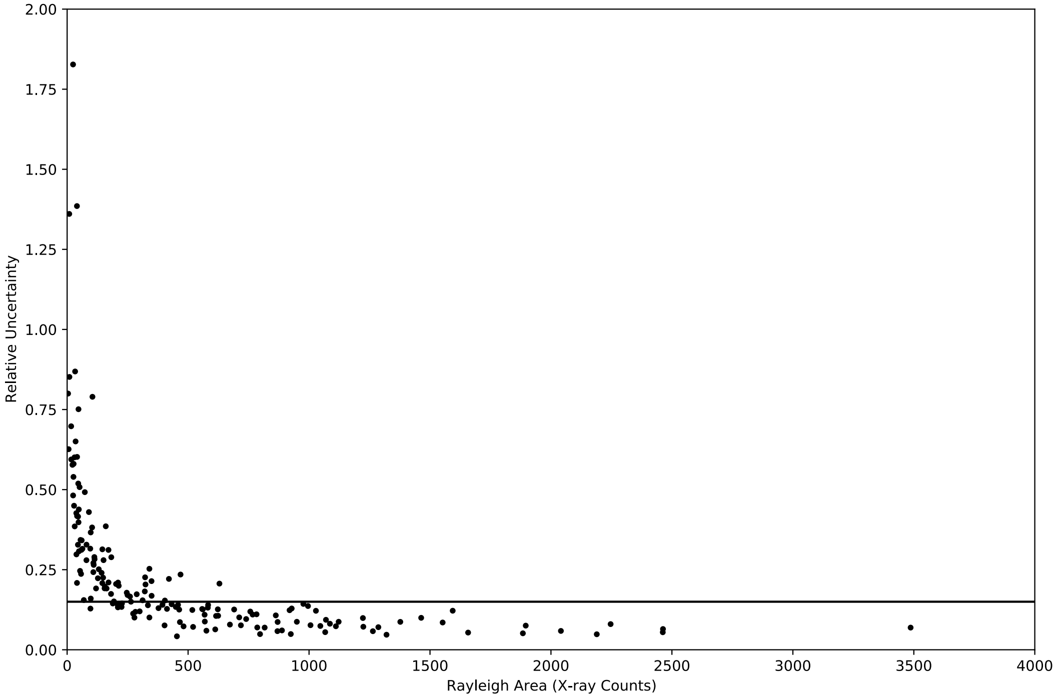

Figure 3.5: Uncertainty of the Compton-to-Rayleigh scatter ratio measurement against area of the Rayleigh peak. A horizontal line is shown at 0.15, above which we have observed the measured standard deviation far exceeds the expected statistical uncertainty. Uncertainty crosses into the well-behaved region at roughly 250 counts.

3.3.2 Comparison with Modeled Ratios

To identify related minerals using the scatter ratio from a single sample, the scatter ratios between them must be distinct, and we need to know the scatter ratio for each option. The most accurate way to determine the expected scatter ratio is to measure a known sample. However, it is not always feasible to measure so many standards. Here we have modeled the spectra for these minerals using PIQUANT and calculated the scatter ratio, shown in Table 3.2. The model gives a good approximation of the ratio and the difference expected between related minerals, but it is not always within error of the measured value.

Table 3.2: Modeled Compton-to-Rayleigh scatter ratios. Experimental ratios here are calculated from the longest duration (least noisy) data for each mineral.

		Model C/R	Experimental C/R
Calcium sulfates	gypsum	3.09	3.10 ± 0.07
	anhydrite	2.38	2.77 ± 0.21
Mg sulfates	hexahydrite	5.59	5.72 ± 0.11
	epsomite	5.74	6.44 ± 0.14
Copper carbonates	azurite	0.89	0.74 ± 0.05
	malachite	0.85	0.70 ± 0.03
Calcium carbonates	calcite	2.47	2.49 ± 0.09
	monohydrocalcite	2.86	2.78 ± 0.04
Mg carbonates	magnesite	6.08	6.71 ± 0.17
	hydromagnesite	6.39	6.97 ± 0.12
Iron minerals	siderite	1.29	1.90 ± 0.11
	hematite	1.67	2.53 ± 0.05
	magnetite	0.79	1.39 ± 0.14

3.4 Discussion

3.4.1 Mineral distinguishability

The longest duration data (2000 seconds) resulted in error bars of less than 10% that were often sufficient to statistically differentiate between minerals otherwise indistinguishable via fluorescence. Of course, distinguishability depends on how different the minerals are. The hydrated copper carbonates (azurite and malachite), for example, have similar compositions. Their average Zs differ by only 4%, and their scatter ratios are also close (6% different), so 10% error is not quite good enough. Across the board, difference in average Z is not a very good predictor of difference in Compton-to-Rayleigh scatter ratio, so it is best to model the expected ratios and see how far apart they are. We have shown that once the statistical uncertainty falls below 15%, it is a good predictor of experimental variation, so anticipated uncertainty is easily calculated based on experimental conditions.

In practice, reaching a few hundred counts in the scattered peaks that is necessary to achieve this level of certainty is quite fast, only a few seconds on a standard XRF instrument. Good measurements can be expected as long as the sample is simple and does not contain combinations of minerals. In this study, we have used a polycapillary optic to reduce the beam diameter, and this substantially reduces the count rate. In a rock specimen, a focused beam allows data to be collected from distinct mineral crystals or grains that are a few hundred microns or larger. Such optics are often used in micro-XRF mapping. An XRF map consists of a series of XRF measurements collected in a line or grid to map element concentrations over a surface. In that case, each measurement is only a few seconds, but there are often hundreds or thousands in the map, and measurements of the same mineral may be summed to create a measurement with longer effective collection time and more counts. A map is expected to take several hours, so long total collection times are not out of the question.

For the most part, modeled ratios were close to the measured ratios, but not quite close enough to be certain about a mineral identification. Eight out of thirteen were within 15% of the measured scatter ratio. In the past, we have observed a trend where the model ratios are systematically lower than measured ratios for low-Z materials, but the PIQUANT software has been updated and that effect is diminished here (O′Neil et al., 2018).

3.4.2 Organic Matter in Shales

As previously noted, light elements such as carbon, hydrogen, and oxygen are particularly associated with life but are undetectable using fluorescence. When an ecosystem develops, organisms eventually die, and their organic matter gets incorporated into sedimentary rocks. Shales form from consolidated mud, and they can include organic matter if present. The composition of shales varies widely, though common components of shales include carbonates, feldspars, and clay minerals. Those with more organic matter are often called "black shales," and they can be 10% or more organic matter, though there is not a precise boundary (Jaffe, 1962; Vine and Tourtelot, 1969). Curiosity Rover findings suggest that mudstone in Gale crater, an ancient lake bed, may contain preserved organic carbon, and the Perseverance rover has landed near an ancient delta in Jezero crater, which may have many similar rock types (Ming et al., 2014).

It would be useful to know whether a shale contains organic matter, and how much, but this is unfortunately not possible from a single measurement given the overall variability of shale compositions, particularly when it comes to clays. Some common components are shown in Table 3.3. Black shales are dark-colored fine-grained rocks that form in a variety of marine or saline lake environments, each with its own chemistry. Therefore, the exact mineral makeup is often unknown. XRF would reveal many elements: Si, Al, Ca, Mg, Na, and could point us toward the major minerals and the scatter ratio could tell us about the lighter elements. However, there is no way to know if lighter elements are in the form of organic matter or clays. For example, K-feldspar and illite have the same florescence peaks and differ only in scatter ratio, so illite is indistinguishable from feldspar plus organic matter. Clay minerals can form abiotically and are not indicative of past life, so do not have the same implications for the past environment as organic matter. If multiple measurements are collected of a rock as part of an XRF map, it may be possible to use heterogeneity to determine organic composition. If we assume clay components are homogenous throughout and organic matter is heterogeneously distributed, excess light elements at some points may be attributed to organic matter.

Table 3.3: Select common components of shales. Limited fluorescence signals combined with a variety of possible feldspar and clay minerals make it impossible to use scatter peaks to learn about organic content of shales.

		Formula	Elements with detectable fluorescence
Carbonates	Calcite Dolomite	$CaCO_3$ $MgCO_3$	Ca Mg
Felspars	K-feldspar Albite Anorthite	$KAlSi_3O_8$ $NaAlSi_3O_8$ $CaAl_2Si_2O_8$	K, Al, Si Na, Al, Si Ca, Al, Si
Quartz		SiO_2	Si
Clay Minerals	Kaolinite Illite Montmorillonite	$Al_2Si_2O_5(OH)_4$ $(K,H_3O)Al_2\ (Si_3Al)O_{10}(H_2O,OH)_2$ $(Na, Ca)_{0,3}(Al,Mg)_2Si_4O_{10}(OH)_2*nH_2O$	Al, Si K, Al, Si Na, Ca, Al, Mg, Si

3.5 Conclusion

The ratio of Compton to Rayleigh scatter reveals the presence of light elements in an XRF measurement that does not directly analyze them. Some mineral identification is possible. It requires both a strong enough signal to confidently calculate the scatter ratio and confidence in the expected value, which can be provided either by measuring a reference mineral or validating a predictive model. Achieving accurate experimental analysis requires 200-300 counts in the Rayleigh peak. Increasing the collection time further can decrease uncertainty to allow discrimination between minerals with more similar average atomic weights. Detecting light elements as organic matter in sedimentary rocks is difficult due to ambiguity in such a rock’s mineral composition, particularly when it comes to clays, but heterogeneities within a rock may offer some information.

Acknowledgements

This work was partially supported by the National Aeronautics and Space Administration as part of the Mars 2020 Project. The support was provided via subcontract 1542830 from NASA's Jet Propulsion Laboratory.

4

OBTAINING BULK-ROCK PROPERTIES FROM MICRO-X-RAY FLUORESCENCE MAPPING DATA

Lauren P. O’Neil, W. Timothy Elam, Joel A. Hurowitz, and David C. Catling

Abstract

X-ray fluorescence (XRF) is a reliable, non-destructive method for measuring elemental abundances in geological samples. Micro-XRF mapping measurements can reveal the spatial relationships between elements and how they are distributed in a sample. However, the bulk-rock properties remain important both inherently for understanding the sample as well as for comparing to other bulk measurements that may exist. Here, a pair of igneous samples (a granite and a diabase) collected from the sites of USGS geochemical reference samples G-1 and W-1 are mapped. Measurements were taken over an 18 mm by 18 mm grid with 1 mm spacing and a 100-micron spot-size. Spectra were analyzed using PIQUANT, x-ray analysis software developed for the Planetary Instrument for X-ray Lithochemistry (PIXL). We have three main findings. First, there are different ways to combine data from a micro-XRF maps to generate bulk elemental abundance. Summing spectra versus averaging quantification results from individual measurements makes negligible difference for major elements but can lead to different values for trace elements. Second, in both rock specimens, a consistent, representative sampling of the bulk rock composition is achieved in 25 spectra, when the variation between measurements has substantially decreased from the variation between single points. Third, information on the mineral components of the rock may be obtained, but it is limited by the grain-size to beam-size ratio.

While results presented here are based on investigation of only igneous samples, there is some applicability to other rock types.

4.1 Introduction

X-ray fluorescence (XRF) is a reliable, non-destructive method for measuring element abundances in geological samples. In Earth sciences, XRF is often selected over other methods because of high precision and low labor requirements, and these same characteristics make it suitable for robotic space missions (Anzelmo and Lindsay, 1987b). XRF uses an x-ray beam to illuminate a sample and quantify the abundance of elements heavier than sodium in the very near surface. It is regularly applied to diverse surface styles, including natural and polished solids, powders, or liquids, and it can provide data on both major and minor elements in a range of matrices (Löwemark et al., 2019).

The Planetary Instrument for X-ray Lithochemistry (PIXL) is part of NASA's Mars 2020 rover, Perseverance. It is mounted on the rover's arm and closely examines Mars' surface from a nominal standoff of 2.55 cm. It is a micro-XRF instrument that uses a small (~100-micron) beam to collect XRF spectra at each point in a grid to provide spatially resolved compositional data in the form of a micro-XRF map (Allwood et al., 2020, 2015). This resolution provides insight into the spatial distribution of elements, but because of heterogeneities, it does not readily provide a single measurement of a rock's bulk composition.

Bulk composition needs to be established for PIXL's results to be put in context, because this is what has usually been measured by other instruments elsewhere on Earth and Mars. Past measurements on Mars have had much lower spatial resolution and much larger analytical spot size, so they provided results that are presumably more representative of the bulk composition. NASA's Curiosity Rover's Alpha Particle X-ray Spectrometer (APXS) can look at a spot of a few centimeters diameter, while Curiosity's ChemCam (which uses laser-induced breakdown spectroscopy) has a minimum spot size of a few hundred microns (Gellert et al., 2006; Lanza et al., 2010). ChemCam's successor on Perseverance, SuperCam, has improved capabilities, but it looks at a similar spot size, as high resolution is not its goal (Wiens et al., 2017). The analytical areas of these instruments are many times the size of a PIXL spot, and they generally analyze only a handful of spots at each site. PIXL's data comes in the context of not only other rover measurements, but also data from orbiters, and the best of these have a resolution measured in meters. The mineralogy of Perseverance's landing site, Jezero Crater, has been analyzed at length from orbit, but on a much larger scale than is achieved by landed instruments, and bulk composition can correct or confirm inferences based on observations made from orbit (Goudge et al., 2015; Horgan et al., 2020). When PIXL collects a micro-XRF map, a bulk measurement can reveal whether it is a rock typical of the region and allow direct comparisons to previous APXS measurements.

Igneous rocks have a variety of grain sizes, ranging from visible mm-scale grains in granites to no grains in amorphous volcanic glasses. The inhomogeneity of the rock leads to inconsistency in measurements. PIXL's smaller beam size is comparable to the grain size of the samples in this study, so a single PIXL measurement has a low probability of encompassing all minerals of such a rock and may only sample one or a few minerals. Furthermore, minerals are not necessarily included in an analytical spot in proportion to their overall prevalence in the bulk rock. Basalts, as are common on the surface of Mars, have grains smaller than those studied here, and this problem would be less pronounced in that case.

The problem of grains is also present in sedimentary rocks, where there is an even greater variety of grain sizes. This has been used as an advantage where the variation between Laser Induced Breakdown Spectroscopy (LIBS) measurements from ChemCam has been used to study grain size, but this same work indicates that bulk composition of Martian sedimentary rocks are not captured by a single ChemCam measurement (Rivera-Hernández et al., 2019). SHERLOC (Scanning Habitable Environments with Raman and Luminescence for Organics and Chemicals), Perseverance's mapping Raman instrument, has comparable resolution and spot size to PIXL, but since Raman is a fundamentally different type of measurement, it is not used to determine a rock's overall composition.

In addition to purposes of comparison, bulk composition is a useful measurement in its own right as a means of understanding the target. Overall abundance of major, minor, and trace elements can be instrumental in determining the conditions under which a rock formed or its history. For example, abundances have been successfully used to make inferences about sand transport and weathering on Mars based on how average composition changes across dunes (O′Connell-Cooper et al., 2018, 2017). Elements associated with mafic minerals in sandstones can also reveal the presence of a magmatic or impact-generated source nearby (Thompson et al., 2016).

Apart from statistical inferences of bulk composition, PIXL's mapping opens up a new class of investigations. Spatially resolved element data can allow characterization of individual components of a sample that are physically interspersed, such as large grains in a fine-grained matrix, crusts on the edge of larger clasts, or distinct layers across the sample. Even qualitative elemental analysis has supported interpretations of ancient rocks and determinations of whether their formation was biologically mediated (Allwood et al., 2018, 2009). While mapping data may allow characterization of individual mineral components of a rock, a drawback of map datasets is that they are time consuming. Data at each point is collected quickly, which leads to low signal-to-noise. If data from a single mineral can be summed across multiple points, signal-to-noise can be improved, and better analysis of particular components is possible. The plausibility of summing in such a manner has not previously been demonstrated, and it is complicated by points that sample multiple minerals or components. Minimum sampling requirements will differ for characterizing the bulk rock versus individual components. Separation and categorization of these components from a large dataset has also been studied, but not on the type of samples used here (Thompson et al., 2015).

The need to generate a bulk measurement from PIXL data raises two questions: 1) how many PIXL spots are needed to get a representative sample of a rock? 2) what happens when we try to combine data from increasing numbers of measurements? This question of sampling has been modeled, but not experimentally tested (McCanta et al., 2017). Here, we seek to address both questions experimentally.

4.2 Experimental

4.2.1 Data Collection

Data were collected for two samples, a granite and a diabase (shown in Figure 4.1) from the same sites as USGS powdered geochemical reference materials G-1 (granite) and W-1 (diabase). These samples provide data for two different grain sizes with similar matrices, known mineralogy, and elements at a range of concentrations.

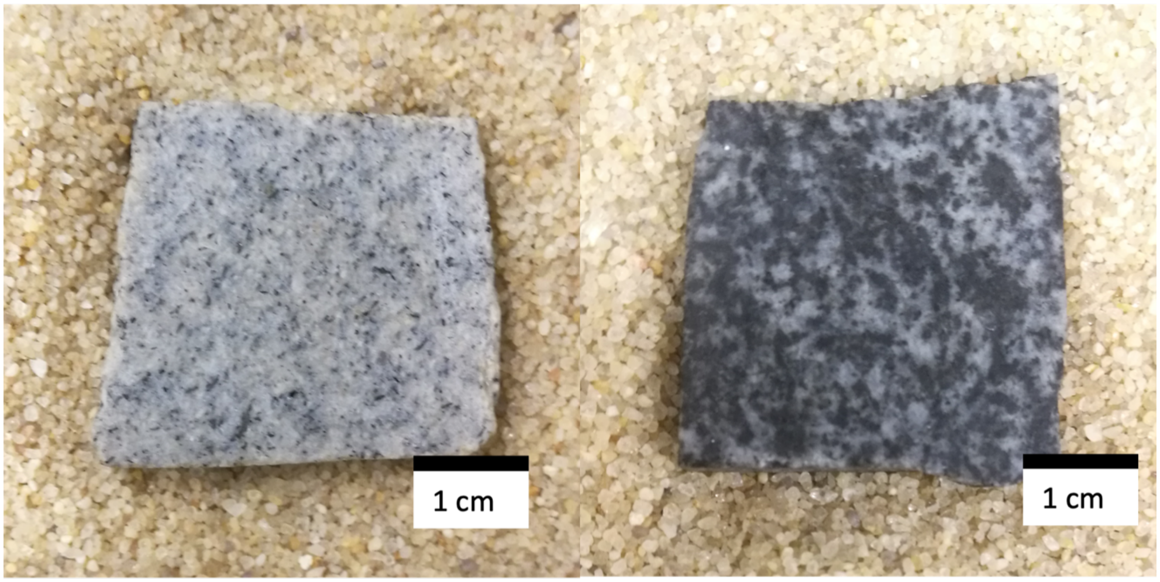

Figure 4.1: Granite (left) and diabase (right) samples from the same sites as USGS powdered geochemical reference materials G-1 (granite) and W-1 (diabase).

Our datasets consist of XRF spectra of 100-micron spots taken in an 18 mm by 18 mm grid with 1 mm spacing as well as a denser 18 mm by 4mm grid with 100-micron spacing. All data were collected in helium with 10 seconds of dwell time per spot and 28 kV 175 µA tube settings. The setup consisted of a Moxtek Rh-anode x-ray source with an XOS polycapillary focusing optic and two Amptek FAST 1-2-3 XDD detectors. Specimens were cut to polished squares roughly 25 mm each side and about 5 mm thick, and the surfaces were measured without further preparation. The denser grid consists of many more points, and statistics are better from that dataset. The sparser grid was used to check whether the spots in the denser grid overlap. If the points had overlapped, the results would be skewed. No difference between results of the datasets was observed, so only results from the denser grid are discussed here.

4.2.2 Data Analysis

Quantification of elemental abundance was performed using an early version of the PIQUANT software developed for analysis of PIXL XRF data based on established equations and parameters (Tertian and Claisse, 1982; Elam et al., 2002). Thirteen elements were investigated: Si, Al, Ca, Fe, K, Mg, Mn, Na, P, Ti, Zr, Ba, and Ce, selected based on anticipated presence in the samples. The software is primarily based on fundamental parameters, and calibration was done with a USGS reference material BHVO-2G, a glass formed from a basalt sample. Use of a single standard is not a rigorous calibration, and therefore results from our measurements of G-1 and W-1 should not be meticulously compared to other values from the literature, but trends and relationships within our datasets are sound.

4.3 Results

4.3.1 Complete dataset

Maps of our two samples are provided in Figure 4.2 and Figure 4.3 for each of the 13 elements analyzed. To find the bulk composition, we first considered the complete datasets, which included all individual spectra for each sample. We employed two different strategies for combining spectra from different points: single-spectrum element concentrations and aggregate-spectrum element concentrations. Single-spectrum element concentrations were generated by processing XRF spectra from 100-micron spots individually using PIQUANT. The resulting element concentrations from many spots can be averaged to represent a larger group. Alternatively, several raw single-spot spectra may be summed to form an aggregate spectrum which is then processed using PIQUANT. Both methods produce element concentrations that represent results from a large set of spectra.

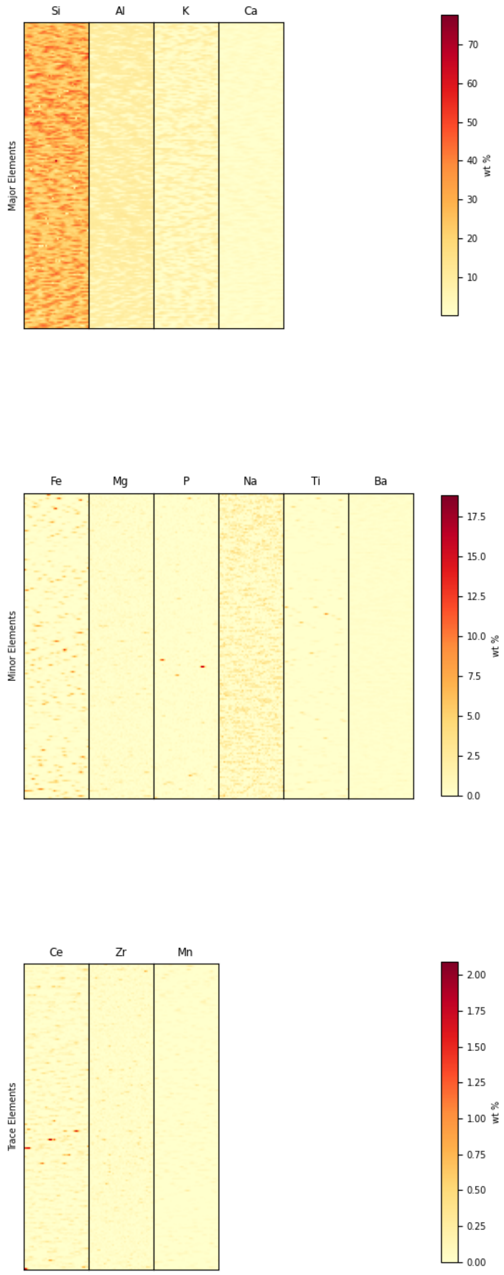

Figure 4.2: Element maps for the granite sample. Data was collected in a 4 mm by 18 mm grid with 100-micron spacing. 13 elements were quantified in each spot, and element distributions are shown. Major, minor, and trace elements are scaled separately.

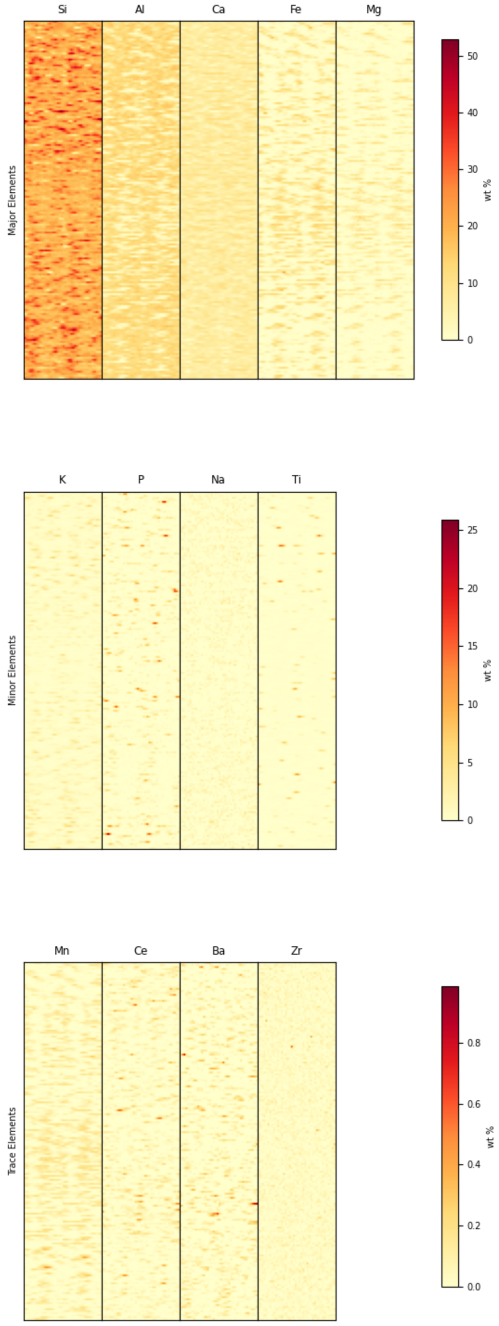

Figure 4.3: Element maps for the diabase sample. Data was collected in a 4 mm by 18 mm grid with 100-micron spacing. 13 elements were quantified in each spot, and element distributions are shown. Major, minor, and trace elements are scaled separately.

We compared the aggregate element concentrations to the averaged single-spectrum element concentrations. Any bias or effect of the combination method will be amplified to its highest level when using the complete datasets, which include over 7000 spots. The results are compared in Table 4.1. We can see a slight difference in results, especially for trace elements, but there is no discernable pattern, and given the variability, it is not significant, as values are within one sigma error bars. For consistency, the remainder of the analysis uses aggregate element concentrations, which is more widely used, and averaged single-spot element concentrations are not considered further.

Table 4.1: Composition using the full dataset. The concentrations of 13 elements known to be in both samples are calculated two ways and shown here as weight percent (Fleischer, 1969). First, the individual spectra are summed to form one aggregate spectrum, and this aggregate spectrum is used for quantification. Second, each individual spectrum is analyzed and then the calculated concentrations are averaged. Both methods use the same data; the difference is in analysis only. Error bars are one standard deviation. For major elements such as silicon and aluminum the results differ by only a few percent, but trace elements vary by more, and in many cases, the difference is statistically significant.

	Granite			Diabase		
	Aggregate	Average	% difference	Aggregate	Average	% difference
Si	37.346	36.5 ± 6.61	2.15	29.664	29.1 ± 4.16	1.62
Al	7.843	7.70 ± 3.00	1.85	11.246	10.6 ± 4.03	5.94
Ca	1.115	1.08 ± 0.91	2.932	7.265	7.23 ± 2.01	0.436
Fe	0.41	0.46 ± 1.18	-11.6	3.129	3.45 ± 3.77	-9.43
K	3.874	3.90 ± 3.14	-0.808	0.797	0.77 ± 0.86	3.22
Mg	0.307	0.25 ± 0.36	22.2	1.925	1.97 ± 2.64	-2.3
Mn	0.004	0.01 ± 0.02	-66.1	0.044	0.04 ± 0.05	-12.5

Na	0.932	0.88 ± 1.06	5.95	0.484	0.54 ± 0.76	-11
P	0.265	0.15 ± 0.50	68.8	0.681	0.62 ± 1.57	9.71
Ti	0.087	0.09 ± 0.34	-12.1	0.274	0.27 ± 0.90	-0.529
Zr	0.021	0.03 ± 0.05	-39.2	0.004	0.03 ± 0.03	-87.5
Ba	0.13	0.10 ± 0.11	23	0.015	0.03 ± 0.06	-54.7
Ce	0.05	0.04 ± 0.10	6.53	0.05	0.03 ± 0.05	53.3

4.3.2 Minimum Sampling Requirement

A map of 7000 spots can take many hours to collect and may not be necessary to characterize the bulk rock. Competing scientific interests and time limitations often lead to shorter measurements with a smaller numbers of spots. To efficiently examine trends in smaller sets of data, we randomly selected subsets of our dataset to simulate smaller measurements. These samples ranged in size from 1 to 50 individual spectra.

First, we looked at trends in elemental concentration as the sample size varies. To reduce statistical noise and properly characterize trends in small sample sizes, we independently selected several samples each of various sizes. Each point on the plots in Figure 4.4 represents the averaged results from 50 samples of the indicated number of spectra. Trends in these plots therefore indicate systematic effects due to the sample size, that is, number of spectra summed per sample. Most element concentrations are consistent with some scatter, which is what we expect. If we look closely at the minor and trace elements, there is some odd behavior. In both samples, zirconium seems to be present at a higher concentration when very few spectra are summed. In the diabase, sodium also increases with fewer summed spectra, but titanium shows the opposite trend. This effect is possibly related to the spatial distribution of these elements in each sample.

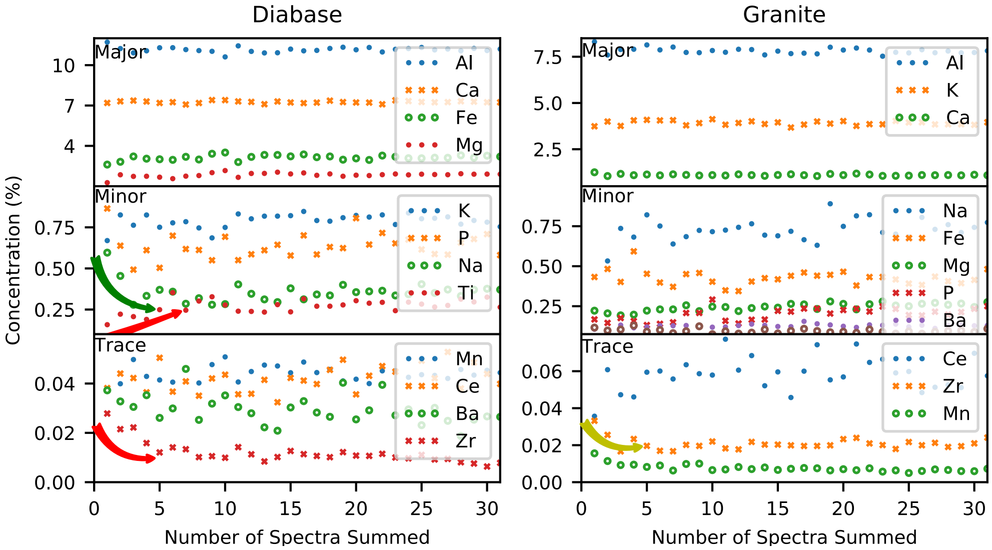

Figure 4.4: Element concentrations. The concentrations calculated from aggregate spectra formed from the sum of an increasing number of individual spectra. To decrease scatter, each data point shown is the average of 50 aggregate elemental concentrations. Silicon is not shown. Many elements show slight drift (either up or down) when fewer points are summed, as indicated by the arrows.

Second, we looked at variability between samples and the number of points it takes to achieve consistent results. To do this, we used the same samples but examined the standard deviation rather than the average across samples of the same size. This is an indication of how much the results are expected to vary from measurement to measurement for various numbers of spots per measurement. The standard deviation is plotted in Figure 4.5 as a fraction of the element's concentration (relative standard deviation).

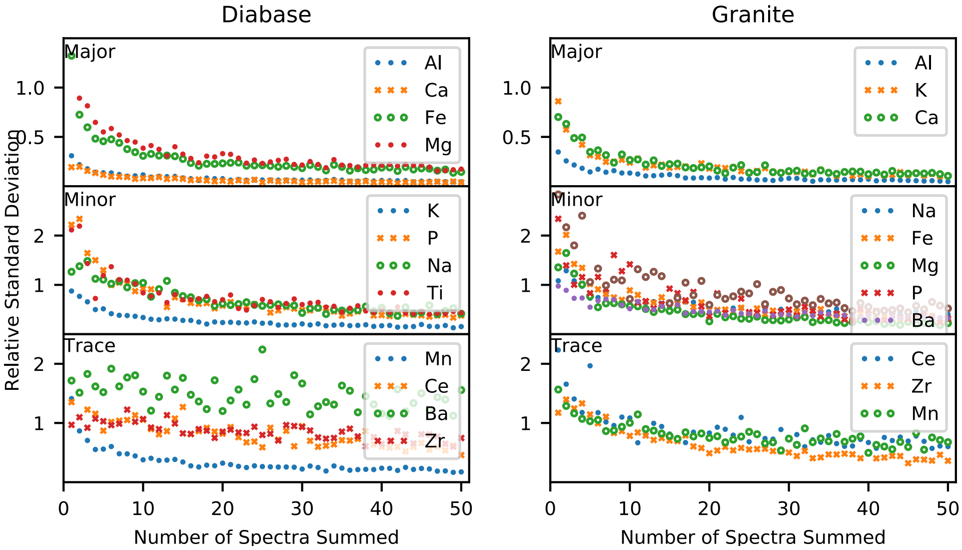

Figure 4.5: Scatter in Measurements. The standard deviation as a fraction of element concentration is plotted against the number of individual spectra included. As expected, when very few spots are included, there is a lot of variability between sets, while they become less varied when more data is included. The standard deviation decreases faster for higher concentration elements. Silicon is not shown.

Figure 4.5 shows that the standard deviation does decrease as we would expect for larger samples, and it decreases faster for elements of higher concentration. The standard deviation for major and minor elements in Figure 4.5 decrease substantially, sometimes by 50% or more, while the trace elements do not. An abundant element such as Si starts out with a much higher signal-to-noise ratio than a trace element such as zirconium; and it is therefore logical that random noise would play a much larger role for lower concentration elements and take more data to overcome. A larger number of points is also required to collect a representative sample of elements when the spatial distribution is more heterogeneous.

When looking at samples that are large compared to the size of the total dataset, it is no longer plausible to assume that all aggregate samples are independent since their constituents are drawn from the same finite pool. Therefore, we did not select random subsets to form samples. Rather, we sort the points into sets of evenly spaced points covering the same interwoven area of the sample rock. For example, a set containing half of the total points includes alternate points, and a set containing a third of the total points includes every third point. So, we generate fewer samples that include high numbers of points. The fractional standard deviations are plotted in Figure 4.6 and go to a much higher number of spots per sample. When adding up to 500 points, the relative standard deviation decreases by a substantially (by a factor of 2 or 3 for most elements), but it does not go down evenly to zero within this range, and the results from the diabase behave similarly.

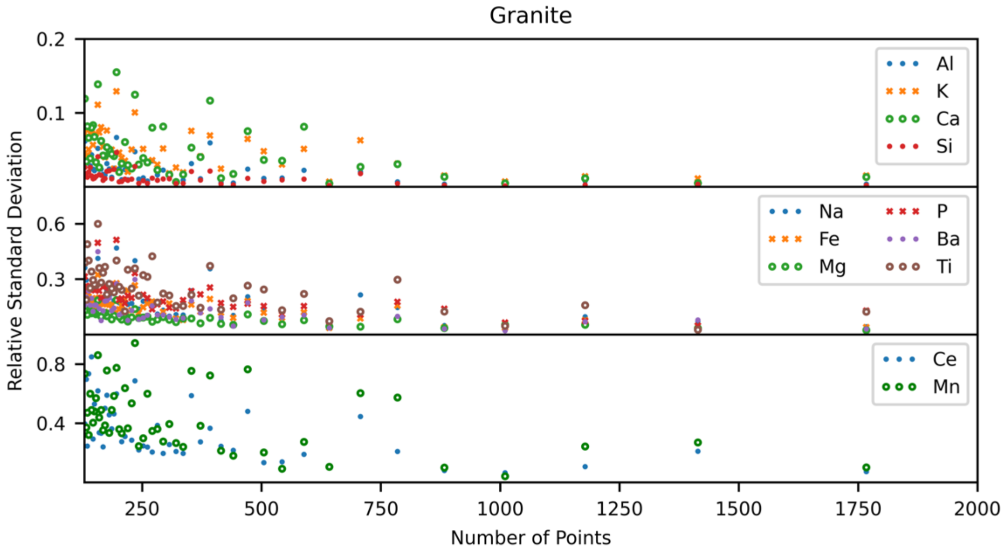

Figure 4.6: Scatter in measurements of the granite sample. The standard deviation between measurements as a fraction of element concentration plotted against the number of points included. After an initial decrease, the relative standard deviation appears to remain constant over most of this range. Zirconium is omitted from the plot because the concentration is very close to the detection limit and is measured to be zero in much of this data, so the relative standard deviation is not meaningful.

4.3.3 Trace Elements and Zero Concentration

The concentrations of trace elements are challenging because they are close to the detection limit. The detection limit for XRF is controlled by whether the fluorescence peaks corresponding to an element can be statistically distinguished from the background, and it can vary between different elements and specimens. The strength of the fluorescence is controlled by how much of the incoming x-ray flux is at an appropriate energy to be absorbed as well as absorption of the elemental fluorescence by other elements in the specimen. The background can contribute noise due to counting statistics and is further complicated by the presence of other fluorescence and diffraction peaks. While it is a small numerical distinction, the difference between an element being present and not present can have significant impact on the scientific interest of a rock, so care should be taken not to lose a signal.

In the granite sample, aggregating spectra rather than averaging results led to a slight increase in the measured concentration of barium and cerium, but a large decrease in the measured concentration of zirconium. The difference in behavior may be associated with a difference in how these elements are distributed in the rock, illustrated in Figure 4.3. Zirconium is present at relatively high concentration in fewer points, and it appears that this type of data is more likely to be lost upon summing spectra. Barium fluorescence, on the other hand, is more widely distributed and so the peak is always close to the noise limit in an individual spectrum. When summing spectra, the noise goes down, which lets the barium fluorescence peak appear clearly.

4.4 Discussion

4.4.1 Combining Spectra

The question of how to combine data is seldom discussed, and it is generally assumed that adding raw spectra is acceptable. For a perfectly homogenous sample, this may be the case. However, here we note that the average single-spot element concentrations may also be used, and that the results can differ slightly. High concentration elements, such as silicon, calcium, and aluminum, had only a few percent difference between methods, so selecting a method is a decision of little consequence for many applications where micro-XRF mapping data is used for mainly qualitative purposes. Element maps have been useful for illustrating layers and facies of sedimentary samples, and the major elements considered are generally high enough concentration that the pattern and special relationships can confidently form the basis for interpretation (Allwood et al., 2009; Hofmann, 1990; Spinks et al., 2010). However, when it comes to doing bulk chemistry where the rock as a whole, rather than different parts, should be characterized, consistent analysis of trace elements is desirable.

There are reasons to suppose one approach might be better than the other based on assumptions in the quantification process. As spectra are added, the effective collection time increases, so the signal-to-noise improves. Therefore, we might expect that results from single spot spectra have larger error and that their average yields a less accurate result than if we had summed the spectra. However, an underlying assumption of the quantification software is that the sample is homogenous. In reality, atoms can interact with and absorb what others emit, and these interelement effects alter the fluorescence signal. A small spot size allows for characterization of a matrix more tailored to each spot's own composition. When spots vary substantially, an average of single-spot element concentrations may be more appropriate. In this case, given that all the minerals present were expected to be mostly silicate, we chose to aggregate spectra. It is easy to imagine that other rocks with other textures may contain grains or crystals of substantially different minerals, such as the Martian “blueberries” which are spherules made of iron oxide (hematite) surrounded by sulfates (Squyres et al., 2004).

Even in the specimens measured in this study (diabase and granite), where the matrix is largely consistent, we see that the distribution of the elements also plays a role, particularly for low concentration elements. It may be the case that the overall concentration of an element is not a useful quantity, but the fact that its concentration is non-zero is scientifically relevant to an investigation. Particular minerals are associated with their constituent elements, and if found can be used for further analysis. Part of the Mars 2020 rover mission is to select samples for future return, and collection for further lab analysis is common on Earth. Zircon grains, for example, are particularly useful in determining the age of a rock. Zirconium concentrated in those grains is exactly the type of information that might be smoothed out by summing large numbers of spectra. Where trace elements are concerned, detections and near detections should not be readily dismissed, and further analysis of the data may uncover critical aspects of a sample.

4.4.2 Minimum Sampling

Several factors contribute to variability between measurements of these igneous samples, including noise and mineral variety. There is photon noise based on counting statistics, and this plays a large role for measurements with small numbers of spots, because the collection time is also very short. The trends in element concentration seen in very low numbers of points in Figure 4.4 is likely due to noise. The sodium fluorescence peak, for example, is generally fewer than 10 counts for a single spot, and often less than 5. While the trend at low sampling count seems odd, it is not outside the error of the concentration obtained from the full data set. Considering that these trends are seen only in low concentrations elements, we conclude that this effect is due to noise and low collection time rather than sampling of the different minerals or components.

Both samples studied have different components made visible by their color: shades of black, white, or gray (Figure 4.1). Knowing that there are areas of different composition, it is not surprising to have variation between spots. Sets of spots that are large enough to characterize the bulk rock should vary only due to noise and should otherwise produce a consistent result. For such subsets selected from this dataset, the variation between measurements is substantially decreased by combining 25 spots, when the standard deviations of a majority of major and minor elements have decreased below 25% of their initial value (Figure 4.5). Each element analyzed has a different concentration and standard deviation, and more measurements may be required for particular scientific goals, especially when it comes to trace elements. Here, 25 spots corresponds to 5 minutes of collection time, which is much less time than the complete 20-hour map. With a 100-micron spot, 25 spots would cover 0.20 mm^2, which does not dwarf the grain size. This indicates that when pushed for time, it may be wise to spread out sampling. These 25 spots were collected over an area of a few square centimeters, but if they were collected all in a row, they might have overrepresented a single large grain. Transects may require more spots to achieve bulk representation because of this problem. It is likely that area covered, as well as number of spots, is a key quantity.

The grain size in the diabase appears to be an order of magnitude larger than in the granite, and yet the averaging results were very similar. This indicates that so long as we are sampling over an area that is much larger than the grains and the beam, the size of the grains relative to the beam does not affect the sampling. Both samples have a similar number of component minerals, and this characteristic may have more bearing on the outcome, though it can be difficult to measure the number of components without a full map. With more components, a greater area may be required to sample all of them. A modeling study found that larger grain size relative to the beam size led to an increased requirement for number of analyses (McCanta et al., 2017). However, the size of the larger grains in the modeling study approached the size of the sample area, whereas here the area sampled was much larger than the grain size.

In general, higher concentration elements start out with lower variability than low concentration elements with few summed spectra and appear to decrease in variability faster with more summed spectra, but this is not a strict rule. Similar to the trace element behavior, this may be due to how these elements are distributed in the sample. Not only is silicon the most abundant, but it is also present in every mineral and spot. Elements such as iron and magnesium are associated with the more mafic minerals, so not only are they lower concentration, they are less evenly distributed, so it takes more sampling to represent them evenly. Some trace elements show steadily decreasing variability with increasing numbers of spots included, while some continue to show large variability even when large numbers of spots are included. In the cases of zirconium and barium this behavior can be tied to the spatial distribution in the specimens.

Granite and diabase are both examples of heterogeneous igneous rocks, but the results can be extrapolated to other rock types. There is no theoretical difference between measuring crystals in an igneous rock and grains in a sedimentary rock with XRF. However, in practice the grains are likely to vary substantially more in sediment. Minerals in an igneous rock have all crystalized from the same melt, so the composition is quite similar. The grains in sediment often have very different sources, and may include silicates, carbonates, oxides, or anything else that happens along. This may make it substantially more heterogeneous. However, an examination of standard deviations such as in Figure 4.5 will still indicate whether it has been sufficiently sampled.

4.5 Conclusion

On homogenous surfaces with very similar minerals, adding spectra can be a powerful way to increase signal-to-noise, but on heterogeneous surfaces the optimal choice is not so clear-cut. Adding spectra versus averaging single-spot element concentrations leads to slightly different results for major and minor elements. Results for trace elements may be slightly different, and these differences may be exacerbated by the element's distribution across the sample area. To achieve a representative bulk result, it is necessary to adequately measure the full range of grain types and minerals present in the specimen. It is thus likely that area covered, as well as number of spots, is a key quantity in deciding on a measurement strategy.

With a 100-micron beam, differences between 25-spot measurements were reduced by a factor of four for a majority of major and minor elements, which indicates 25 spots is sufficient to represent a bulk composition of the rock, and adequately sample all minerals present. This result suggests that bulk chemistry can be determined from a micro-XRF mapping dataset and that it is likely that different components, such as stratigraphic layers or large spherules, will also have sufficient coverage to be characterized. We found the same bulk-composition result for each specimen despite their different grain sizes, but characterization of individual components is limited by the relative size of the beam and grains.

5

EFFECTS OF MATRIX STRUCTURE ON X-RAY FLUORESCENCE (XRF) MEASUREMENTS: CONSISTENCY IN SULFUR QUANTIFICATION

L. P. O'Neil, W. T. Elam, and D. C. Catling

Abstract

This paper examines the discrepancies in measured concentrations of sulfur based on its spatial distribution in a specimen. We focus on sulfur in geologic samples, but other sample types, such as in art or archaeology may have similar difficulties. Samples analyzed with x-ray fluorescence (XRF) are assumed to be homogenous, particularly if their structure is on the scale of microns, which is smaller than the analytical spot and often invisible to the eye. However, x-ray interactions do occur on this scale, so structures can alter measurements. Here, we simulate XRF spectra with different structures and examine the effect of micron-scale sulfate layers and coatings. We found that coatings of salts and carbonate have only a moderate effect (less than 15%) on quantification, but we saw thick coatings of hematite, a very dense material, have a greater impact, diminishing the sulfur signal up to 85% in this study. Structural interference can be mitigated by extensive grinding as part of sample preparation.

5.1 Introduction

5.1.1 Role of sulfur on Mars

Sulfur on Earth is accumulated on the surface by volcanic outgassing. On prebiotic Earth, sulfur likely existed as H_2S and SO_2, and may have been involved in the origin of life (Domagal-Goldman et al., 2016; Olson and Straub, 2016). H_2S was an important microbial energy source before the rise of O_2 in the atmosphere, and it remains important to metabolism and signaling in organisms today. A change of sulfur between oxidized and reduced states (e.g., reduction of sulfate to elemental sulfur or sulfide) is a potential source of metabolic energy for microbes if life once existed in sulfate-rich waters on Mars, which lacks Earth's atmospheric O_2 (Pontefract et al., 2017). Such microbial sulfate reduction would impart potentially detectable isotopic fractionation of sulfur. Speculatively, a sulfur-based metabolism has been proposed to support life in Venus' clouds (Limaye et al., 2018). Sulfur's close association and importance to life makes it an element of interest on other planets.

Sulfur is far more abundant on Mars than on Earth's land surface, and it is important for interpreting Mars' geological history. In Mars' regolith, sulfur is typically present at ~1.3 weight %, and in the past, sulfur participated in aqueous, atmospheric, and volcanic processes (Clark et al., 1976; King and McLennan, 2010). Regolith consists of the unconsolidated soil, sediment, and rock fragments that overlie bedrock. High sulfate concentrations can arise from low pH surface waters, and the abundance of hydrous sulfates on Mars' surface, in particular, is consistent with acidic conditions during the last 3.7-3.5 billion years of Mars's history (Bibring et al., 2006; Gaillard and Scaillet, 2009). In the past, Mars was volcanically active and volcanic SO_2 would have impacted the climate. Although SO_2 is a greenhouse gas (Halevy et al., 2007), the net effect of volcanic sulfur is to cool the planet because of the formation of sulfate aerosols that reflect sunlight (Smith et al., 2014; Tian et al., 2010). In the case of high rates of volcanism, Mars' atmosphere would have been driven anoxic, leading to both elemental and sulfate particles forming and falling to the surface, acting as potential tracers of the early environment's redox state (Sholes et al., 2017). Martian magmas are S-rich compared to Earth, and this S can change the partitioning of other elements in a melt, thereby altering the availability of several other elements on Mars' surface (Usui et al., 2022).

Given the importance of sulfur for evaluating Mars' past environment and its astrobiological potential, correct detection and quantification of sulfur is essential. Here, we characterize the magnitude of the interference caused by salts and sulfate coatings around small grains in XRF measurements.

5.1.2 Quantification and element distribution

Current XRF quantification methods and software assume that samples are homogenous; that is, they assume that all elements in the specimen are evenly distributed throughout the sample. This is an acceptable assumption when dealing with glass beads or otherwise homogenized samples, but it may be an issue with powdered specimens and is a particular problem for minimally prepared or natural surfaces. In an XRF measurement, we measure the intensity of fluorescence emitted by each element, but this emission must pass through the rest of the sample and may be absorbed by the matrix. We therefore need to be aware of a matrix effect, i.e., the effect of other components in the sample besides the one we wish to measure. The separation of the elements into different mineral crystals or grains may cause the signal to experience substantially different matrix effects than we assume. This causes the measurement to be systematically inaccurate and has proved particularly troublesome in quantification of sulfur in sedimentary settings. It is possible that small crystals or grains are coated by salts present in the specimen, and that this systematically shields and diminishes the measured fluorescence signal of analytes in the grains.

Alpha Particle X-ray Spectrometer (APXS) instruments have previously flown on NASA's Mars rovers Sojourner, Spirit, Opportunity, and Curiosity (Gellert and Yen, 2019; Rieder et al., 1997), but Mars Perseverance Rover carries the Planetary Instrument for X-ray Lithochemistry (PIXL), an XRF instrument. APXS uses a combination of Particle Induced X-ray Emission spectroscopy (PIXE) and XRF to quantify elemental abundances, and it is subject to the same limitations and assumptions about sample homogeneity as XRF (Campbell et al., 2009). PIXE has been shown to be accurate to within a few percent for major and minor elements (Heirwegh et al., 2016; Johansson, 1989). Calibration difficulties with sulfur due to heterogeneity have been encountered by the Curiosity Rover's APXS (Campbell et al., 2012). A study evaluating APXS measurements found that sulfur abundances were systematically high compared to gravimetric sulfur concentrations, sometimes up to 30% (Berger et al., 2020). Not all inconsistencies are due to distribution of elements, and grain size distribution has been shown to interfere with iron quantification (Flannigan and Campbell, 2017).

Assuming a homogenous sample is common because the alternative is computationally difficult. The two main quantification methods are fundamental parameters or Monte Carlo. The fundamental parameters method is more widely used, but Monte Carlo can accommodate more complex sample configurations (Gardner and Doster, 1978). Monte Carlo software has been developed for particular applications, such as confocal micro-XRF (Czyzycki et al., 2011). To apply more generally, a Monte Carlo code was developed and made available based on layers (Schoonjans et al., 2012; Vincze et al., 1993). Layers have been a part of quantification efforts in fields such as cultural heritage and art, where the specimen typically must be measured without destruction, and layers of material, such as paint, are commonplace, though not entirely without destruction (Brunetti et al., 2016, 2015; Mantler and Klikovits, 2004; Mantler and Schreiner, 2001). Layers can be a good approximation of complicated surfaces even when the boundaries between layers are not clean, such as in the case of corrosion (Mortazavi et al., 2022; Schiavon et al., 2016).

5.2 Methods

5.2.1 Sediment Composition

We focused on sulfur-bearing minerals and examined the effects of nearby minerals on sulfur measurements. We used a computer model to simulate measurements for three rock types: organic-rich lake sediment, marine sediment, and Martian soil. The lake sediment and marine sediments have been selected to represent common silicates where sulfur quantification has been problematic. Additionally, such coatings as investigated here are likely to form in aqueous environments. Light-weight organic matter is a substantially different matrix which is of particular astrobiological interest, but does not represent the majority of sediments, so two sediment materials were investigated. Martian regolith is characterized by different salts than most terrestrial soils and so was also included. The bulk composition for each is shown in Table 5.1.

Table 5.1: Elemental composition for each matrix in weight percent.

	Lake sediment	Marine Sediment	Martian Regolith
Si	19.46	19.53	21.64
Ti	0.2397	0.8391	0.5216
Al	3.123	7.505	3.170
Fe	2.868	7.666	10.59
Mn	0.0774	1.750	0.2478
Mg	0.5427	1.954	5.186
Ca	1.286	3.345	4.531
Na	0.5193	4.295	1.113
K	0.6641	2.241	0.1827
P	0.1309	0.5499	0.1789
S	0.3965	0.1161	2.745
C	46.30	11.26	0.0
H	0.0	0.0	0.0
Cl	0.0	0.0	0.3781
Cr	0.0033	0.0078	0.1197
O	28.19	38.30	49.85

The sediment compositions are based on standards because these are often used in calibration efforts where accurate and precise quantification is particularly important. The lake sediment chemistry is based on LKSD-4, a standard collected by the Geological Survey of Canada. It is a lake sediment composite from Big Gull Lake in Ontario and Key and Sea Horse Lakes in

Saskatchewan (Lynch, 1999, 1990). The marine sediment is based on JMS-2, a standard from the Geological Survey of Japan. It is a deep-sea marine sediment mixture from several locations in Penrhyn Basin, South Pacific. It is mainly pelagic clay with many crystals and zeolite aggregates, and gypsum and hematite have been detected (Terashima et al., 2002). We have fixed the concentrations where there is ambiguity or uncertainty, which is particularly common for volatiles and organic components, to completely specify a composition for our calculations. Trace elements below 0.1 weight percent are excluded except where necessary to form our minerals of interest. The Martian soil composition is based on an average of Alpha Particle X-Ray Spectrometer (APXS) data from 28 basaltic soils in Gusev crater tabulated by Yen et al., with soil mineralogy informed by McSween et al. (McSween et al., 2010; Yen et al., 2005).

5.2.2 Modeled Structures

We simulated a layered structure to model the behavior of sulfate grains in each sediment type. We modeled the calcium sulfate ($CaSO_4$) as a 2-micron layer (2.81 g/cm^3) and placed it under 0.001 g/cm^2 of sediment, which is approximately 5 microns deep in compacted sediment, depending on the density. Pore space is invisible to XRF, so the relevant quantity in the simulation is mass per area, and we can ignore variations in sediment density and volume. The thickness and depth were chosen based on the penetration depth of sulfur fluorescence. We aimed to have the sulfate layer be detectable while including substantial sediment in the x-ray's path. For reference, sulfur K_α fluorescence is at 2.3 keV, which is 90% blocked by 7.23 microns of quartz (SiO_2). Putting the sulfate this close to the surface enhanced the measured sulfur and ensured differences would be measurable. Additional layers were added below, spaced to maintain the overall concentration of sulfur up to a depth of 5 to 20 mm to ensure consistent behavior of higher energy parts of the XRF spectrum. This scheme is show in Figure 5.1.

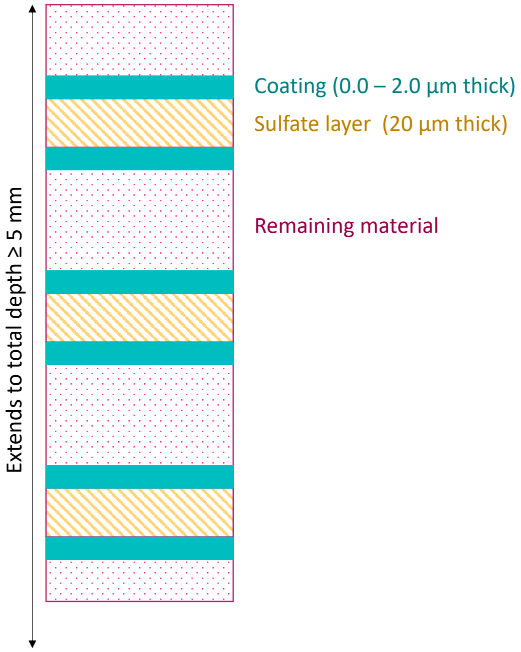

Figure 5.1: Simulated configurations. The sulfate layers are 20 μm thick and are spaced such that all the sulfur is removed from the remaining material and the average composition overall is maintained. The sulfur layers are coated with calcium carbonate ($CaCO_3$) in the lake sediment, hematite (Fe_2O_3) in the marine sediment, and salt ((Na, K) Cl) in the Martian soil. When the coatings are added, this material is subtracted from the remaining material to maintain average concentrations. Simulations were done with a coating of thickness 0, 0.2 nm, and 2 μm except for the Martian soil, which was limited to a maximum coating thickness of 0.08 μm by Na and K availability. The thickness of the top layer of coating and remaining material combined was kept constant to minimize the impact of distance on the sulfur quantification.

Four simulations were done for each sediment type. First, a homogenous mixture used for calibration of the model, and then three with a layered structure. Case 1 consisted of bare sulfur layers in sediment with a coating thickness of 0. In case 2, a thin coating (0.2 nm thick) is layered directly above and below the sulfate layer. This material is subtracted from the sediment, so the total mass and composition remains the same, but some components are in layers rather than mixed evenly. In case 3, a thicker coating is layered around the sulfate layer, up to 2 μm, limited by the availability of the component elements. It is possible that finer-grained sediment particles end up coating larger sulfate particles by adsorption, so a coating does not need to have formed directly on the sulfate crystal.

In the lake sediment, we use layers of calcium carbonate ($CaCO_3$), in the marine sediment, we examined hematite (Fe_2O_3). This combination provides a strong contrast between two minerals with very different x-ray absorption properties. A hematite coating is not particularly likely, but represents highly dense minerals, an important endmember. In the Martian soil, we used chloride salt, (Na, K) Cl. Martian soil is much higher in chlorine than the terrestrial sediments, and its effects can therefor only be explored there. Salts also are more likely to form around the sulfate grains as opposed to adsorbing on, so the thin coating is more likely for this type of mineral.

5.2.3 Software: PIQUANT and XMI-MSIM

Model spectra were generated using XMI-MSIM. XMI-MSIM is a Monte Carlo model, and the underlying algorithms have been previously described (Schoonjans et al., 2012; Vincze et al., 1995, 1993). Monte Carlo models are preferred for complex structures because they handle higher order interactions and can be widely adapted to different geometry.

Quantification was done with PIQUANT version 3.2.6. This x-ray analysis software, developed for the Planetary Instrument for X-ray Lithochemistry (PIXL), is a fundamental parameters model representative of commercially available quantification software. It is based on fluorescence calculations from Tertian and Claisse, x-ray tube calculations from Ebel, scattering calculations from van Sprang and Bekkers and constants and data from a database previously published by Elam (Ebel, 1999; Elam et al., 2002; Sprang and Bekkers, 1998; Tertian and Claisse, 1982). We simulated spectra for homogenous versions of each sediment, and we used these spectra to calibrate the quantification software.

5.2.4 Modeled Instrument parameters

The setup modeled was very simple to ensure that effects are due to the configuration of elements in the specimen rather than difficulty in modeling the instrument. We selected a parallel beam x-ray tube with silver anode run at 40 keV and 40 μA. We simulated a 100-micron beam run in a vacuum with the incoming beam at a 45-degree angle to the surface. The detector was a silicon drift detector with a 0.002 cm Be window and collected at a 45-degree angle from the surface, 90 degrees from the incoming beam.

5.3 Results

5.3.1 Sulfur Quantification

Sulfur quantification for each of the sediments is given in Table 5.2. The thin coating appears to have had a small effect (up to 13%), and the thick coating made a particularly large difference in the marine sediment.

Table 5.2: Measured sulfur concentrations, in weight percent.

	Lake Sediment	Marine Sediment	Martian Regolith
No Coat	9.22	6.56	5.28
Thin coat	10.46	6.54	5.27
Thick coat	10.48	0.97	5.32

The lake sediment contained a sulfate layer sandwiched between carbonate ($CaCO_3$) layers. Rather than shielding the sulfur fluorescence from the detector, it has slightly increased the apparent concentration. This may be the effect of the light-weight carbonate. Carbon and oxygen fluorescence is invisible, and has substantially changed the matrix, leading to an increase in measured concentrations of all detected elements.

In the marine sediment, we study hematite (Fe_2O_3). This simulation behaved as expected. The thin coating has a minimal effect, and a thicker crust absorbed and blocked sulfur fluorescence.

In the lake and marine sediments, the crust thickness was limited to 2 microns. In the regolith simulation, there is only enough salt to form a crust of 0.08 microns, which is much thicker than the 0.0002 microns of the thin coating, but still much less than the others. As we see in **Table 5.2**, it appears to have had very little effect and measured sulfur variations are within 1%.

5.3.2 Depth and limitations of Monte Carlo

The Monte Carlo model used to generate spectra was limited to 4 interactions per photon; a photon that is absorbed and emitted deep in the sediment may be absorbed and re-emitted or scattered only a limited number of times before the calculation ceases. Simulations limited to 3 versus 4 interactions yielded negligible differences (up to about 0.01%), so we are confident that further interactions are not necessary. This is particularly relevant to the lake sediment simulations. When sulfur is surrounded by carbonate, its immediate neighbors (carbon atoms) are slightly less likely to absorb x-rays than the silicon and trace elements in the bulk, and there was concern that only initial interactions would include more scattering as x-rays make their way through the carbonate layer, and then the simulation would stop simulating interactions in the top layer. However, re-absorption as the x-rays travel through the top layer does not seem substantially different.

5.4 Discussion

5.4.1 Real variability in specimens

For many applications of XRF, homogeneity is a good assumption. In measuring alloys or when the sample has been homogenized by melting or other means of preparation, elements can be assumed to be evenly distributed and good, consistent quantification obtained (Ghidotti et al., 2021; Mzyk et al., 2002). In other applications, it is clearly not a good assumption, and steps have been taken to account for layers of gilded metals or pigments (Ager et al., 2019; Cesareo et al., 2010, 2008; Manso et al., 2019). As a field, geology includes materials of both varieties, and it is not always clear which to expect. Obsidian, a volcanic glass, is often used for calibration because it is naturally mixed (Martindale Johnson et al., 2021). Sedimentary rocks often consist of particle and grains with different sources and compositions, which can vary subtly, as in different grains of sand, or substantially, if a bone fragment or other material gets included. In between these extremes are rocks with well-mixed mineral components that have been altered by water or weathering and developed crusts or weathering rinds. These are the ones we seek to address here.

In order for a specimen's structure to be relevant to XRF quantification, it must vary within the volume illuminated by the beam. Higher energy x-rays penetrate further than others, and the energy of the lines used to quantify major and minor elements in a rock are typically below 10 keV, which have a penetration depth up to about 450 microns in quartz. Only structures smaller than this will impact quantification. It is common for grains to be this size; geologists have a slew of terms for describing and categorizing rocks with small grains – mudstone, shale, silt, etc.

5.4.2 Overall effect of coatings

By themselves, the coating, regardless of thickness had only a moderate impact (less than 15%) on the detected sulfur except in the marine sediment, where the coating was iron oxide. This suggests that the matrix effects are limited, should have only modest interference with quantification. Calcium carbonate had a much smaller effect than iron oxide, reducing the sulfur signal by only 14% as opposed to 85%. We attribute this to the density and strong absorption of iron. Minerals with these properties may be cause for concern. However, the effects would be tempered by any degree of hydration, so a pure coating of a concentrated mineral with a heavy cation is not likely given their overall abundance in rocks and soils. During calibration, PIXL, the XRF instrument included on NASA's Perseverance rover, saw discrepancies of 18 and 23% in sulfur quantification in LKSD-4 and JMS-2, and coatings could account for this.

5.4.3 Sulfur distribution

The matrix effect seems able to account for some differences in sulfur quantification, but we suggest that a coating may also substantially alter the position of sulfur in a sediment, which we have not explored here. One of the consequences of sulfur being in a concentrated grain is that less is distributed on the surface (top few microns). If an analyte is well mixed in the sample and not likely to form grains, obviously this is a nonissue. On the other hand, if the analyte is present as part of a salt or secondary mineral that has seeped into the rock, it is likely to be segregated, and this holds true for both natural and powdered samples if the grains are not ground to a sufficiently small size. While the matrix effect may not hide the sulfur by itself, being surrounded may sequester it below the immediate surface. For sulfur, the primary means of quantification is the K_α line at 2.3 keV. In a pure SiO_2 matrix with a density of 2.65 g/cm^3 (typical of quartz), 90% of sulfur fluorescence is blocked by 7.23 microns. A natural soil or powdered sample will have gaps and pore space, so the penetration depth is greater in practice, but a coating of a few microns will move sulfur, on average, that much further from the surface and will appear less abundant.

Sulfate is likely to interact with the surrounding rock and these issues are a real concern. In soils, sulfate is known to adsorb to a variety of surfaces, which may lock it away from the surface where it is exposed to x-rays (Sadeghalvad et al., 2021). Alternatively, sulfate may cement a duricrust in the Martian regolith, which could enhance its detection (Clark et al., 1977). In natural samples, an understanding of aqueous processes may be required for interpreting measured sulfur abundance. In powdered samples, extra care should be taken in grinding to a sufficiently small grain size that it is evenly homogenized.

Some of these heterogeneities might be addressed by supporting data in a micro-XRF map dataset, such as those collected by PIXL. Such data sets may reveal associations between elements, and therefor minerals that are present together across a surface. This information would inform what processes have acted on the sulfate and show the distribution of sulfate grains.

5.5 Conclusion

As we have seen here, the concentration of elements into grains and coatings on the scale of a few microns has a substantial impact on quantification (up to 85% difference), and no easy solution. Even very thin coatings altered results by up to 13%. This can be addressed by using standards with a similar grain structure or sample preparation, but where that is not possible, one can only be mindful of the limitations of XRF quantification. Extensive grinding of powdered samples may also help disassemble micron-scale structures. It is possible that the separation between sulfate and the surface may be an additional factor in quantification.

6

CONCLUSION

Here, we have pushed to glean as much information as possible from limited XRF data. We have done so by establishing new analytical methods and exploring their limitations. This will increase the science return of PIXL and other XRF instrumentation, particularly in geologic settings.

In Chapter 2, we established a method for reliable measurement of the scatter ratio. We analyzed a fluorescence peak generated in the x-ray tube that is duplicated in the measured spectrum by scattering in the sample. These peaks have very low signal strength compared to the background, so removal of the background continuum is carefully done with an empitacle algorithm. The Rayleigh peak is fit with a sum of gaussians, and the Compton scattered peak area is determined empirically due to its nonstandard shape. This method produces a reliable and consistent measurement of the Compton to Rayleigh scatter ratio that can be predicted with a model such as PIQUANT, though a correction factor may be necessary.

In Chapter 3, we determined the guidelines for using the scatter ratio to distinguish between minerals. When the area of the Rayleigh peak dropped below a few hundred counts, additional error beyond statistics appeared in the method. Modeling the spectrum using PIQUANT provides a good estimation of statistical error that can be expected, but the model is not accurate enough to identify each mineral based on a single measurement. Therefore, a standard must be measured to determine the scatter ratio of potential mineral identities.

In Chapter 4, we used micro-XRF maps to determine bulk composition. We found that different ways of combining spectra may yield slightly different results, though not significantly so for major elements. For both samples analyzed, we found that 25 measurements considerably improved the representation of mineral components and provides reasonably consistent quantification of major and minor elements despite their difference in grain size. The measurements should be spaced over an area larger than the grain size to get a representative sampling. When the beam is small enough to hit single minerals, it is also possible to characterize individual components of the rock.

In Chapter 5, we examined the impact of small-scale heterogeneity on sulfur quantification. We look specifically at the effects of coatings around sulfate grains and the matrix effect. We found that for carbonate and salts, the effect was moderate (up to 14%), and for very dense coatings it can be as high as 85%, but these types of coatings are not likely. Further study is warranted on the impact of coatings on the arrangement and distance from the surface of sulfate grains in different circumstances.

7

REFERENCES

Ager, F.J., Respaldiza, M.A., Scrivano, S., Ortega-Feliu, I., Kriznar, A., Gómez-Tubío, B., 2019. Cultural heritage science at CNA (seville, Spain): Applications of XRF and IBA techniques to art and archaeological objects. Radiation Physics and Chemistry. https://doi.org/10.1016/j.radphyschem.2019.05.014

Allwood, A., Clark, B., Flannery, D., Hurowitz, J., Wade, L., Elam, T., Foote, M., Knowles, E., 2015. Texture-specific elemental analysis of rocks and soils with PIXL: The Planetary Instrument for X-ray Lithochemistry on Mars 2020, in: 2015 IEEE Aerospace Conference. Presented at the 2015 IEEE Aerospace Conference, pp. 1–13. https://doi.org/10.1109/AERO.2015.7119099

Allwood, A., Wade, L., Foote, M., Elam, W., Hurowitz, J., Battel, S., Dawson, D., Denise, R., Ek, E., Gilbert, M., King, M., Liebe, C., Parker, T., Pedersen, D., Randall, D., Sharrow, R., Sondheim, M., Allen, G., Arnett, K., Zimmerman, R., 2020. PIXL: Planetary Instrument for X-Ray Lithochemistry. Space Science Reviews 216. https://doi.org/10.1007/s11214-020-00767-7

Allwood, A.C., Grotzinger, J.P., Knoll, A.H., Burch, I.W., Anderson, M.S., Coleman, M.L., Kanik, I., 2009. Controls on development and diversity of Early Archean stromatolites. Proceedings of the National Academy of Sciences 106, 9548–9555. https://doi.org/10.1073/pnas.0903323106

Allwood, A.C., Rosing, M.T., Flannery, D.T., Hurowitz, J.A., Heirwegh, C.M., 2018. Reassessing evidence of life in 3,700-million-year-old rocks of Greenland. Nature 563, 241–244. https://doi.org/10.1038/s41586-018-0610-4

Anzelmo, J.A., Lindsay, J.R., 1987a. X-ray fluorescence spectrometric analysis of geologic materials Part 1. Principles and instrumentation. J. Chem. Educ 64, A181.

Anzelmo, J.A., Lindsay, J.R., 1987b. X-ray fluorescence spectrometric analysis of geologic materials Part 2. Applications. J. Chem. Educ 64, A200.

Bandfield, J.L., 2002. Global mineral distributions on Mars. J.-Geophys.-Res. 107, 9–1. https://doi.org/10.1029/2001JE001510

Berger, J.A., Schmidt, M.E., Campbell, J.L., Flannigan, E.L., Gellert, R., Ming, D.W., Morris, R.V., 2020. Particle Induced X-ray Emission spectrometry (PIXE) of Hawaiian volcanics: An analogue study to evaluate the APXS field analysis of geologic materials on Mars. Icarus 345, 113708. https://doi.org/10.1016/j.icarus.2020.113708

Bevington, P.R., Robinson, D.K., 2003. Data Reduction and Error Analysis for the Physical Sciences, 3rd ed.

Bibring, J.-P., Langevin, Y., Mustard, J.F., Poulet, F., Arvidson, Raymond, Gendrin, A., Gondet, B., Mangold, N., Pinet, P., Forget, F., Berthé, M., Bibring, J.-P., Gendrin, A., Gomez, C., Gondet, B., Jouglet, D., Poulet, F., Soufflot, A., Vincendon, M., Combes, M., Drossart, P., Encrenaz, T., Fouchet, T., Merchiorri, R., Belluci, G., Altieri, F., Formisano, V., Capaccioni, F., Cerroni, P., Coradini, A., Fonti, S., Korablev, O., Kottsov, V., Ignatiev, N., Moroz, V., Titov, D., Zasova, L., Loiseau, D., Mangold, N., Pinet, Patrick, Douté, S., Schmitt, B., Sotin, C., Hauber, E., Hoffmann, H., Jaumann, R., Keller, U., Arvidson, Ray, Mustard, J.F., Duxbury, T., Forget, François, Neukum, G., 2006. Global Mineralogical and Aqueous Mars History Derived from OMEGA/Mars Express Data. Science 312, 400–404. https://doi.org/10.1126/science.1122659

Boehnhardt, H., Bibring, J.-P., Apathy, I., Auster, H.U., Ercoli Finzi, A., Goesmann, F., Klingelhöfer, G., Knapmeyer, M., Kofman, W., Krüger, H., Mottola, S., Schmidt, W., Seidensticker, K., Spohn, T., Wright, I., 2017. The Philae lander mission and science overview. Phil. Trans. R. Soc. A. 375, 20160248. https://doi.org/10.1098/rsta.2016.0248

Brunetti, A., Depalmas, A., di Gennaro, F., Serges, A., Schiavon, N., 2016. X-ray fluorescence spectroscopy and Monte Carlo characterization of a unique nuragic artifact (Sardinia, Italy). Spectrochimica Acta Part B: Atomic Spectroscopy 121, 18–21. https://doi.org/10.1016/j.sab.2016.04.007

Brunetti, A., Golosio, B., Schoonjans, T., Oliva, P., 2015. Use of Monte Carlo simulations for cultural heritage X-ray fluorescence analysis. Spectrochimica Acta Part B: Atomic Spectroscopy 108, 15–20. https://doi.org/10.1016/j.sab.2015.03.014

Campbell, J.L., Lee, M., Jones, B.N., Andrushenko, S.M., Holmes, N.G., Maxwell, J.A., Taylor, S.M., 2009. A fundamental parameters approach to calibration of the Mars Exploration Rover Alpha Particle X-ray Spectrometer. J. Geophys. Res. 114, E04006. https://doi.org/10.1029/2008JE003272

Campbell, J.L., Perrett, G.M., Gellert, R., Andrushenko, S.M., Boyd, N.I., Maxwell, J.A., King, P.L., Schofield, C.D.M., 2012. Calibration of the Mars Science Laboratory Alpha Particle X-ray Spectrometer. Space Sci Rev 170, 319–340. https://doi.org/10.1007/s11214-012-9873-5

Campbell, J.L., Perrett, G.M., Maxwell, J.A., Nield, E., Gellert, R., King, P.L., Lee, M., O'Meara, J.M., Pradler, I., 2013. Refinement of the Compton–Rayleigh scatter ratio method for use on the Mars Science Laboratory alpha particle X-ray spectrometer. Nuclear Instruments and Methods in Physics Research Section B: Beam Interactions with Materials and Atoms 302, 24–31. https://doi.org/10.1016/j.nimb.2013.03.006

Cesareo, R., Brunetti, A., Ridolfi, S., 2008. Pigment layers and precious metal sheets by energy-dispersive x-ray fluorescence analysis. X-Ray Spectrom. 37, 309–316. https://doi.org/10.1002/xrs.1078

Cesareo, R., Calza, C., Dos Anjos, M., Lopes, R.T., Bustamante, A., Fabian S., J., Alva, W., Chero Z., L., 2010. Pre-Columbian alloys from the royal tombs of Sipán; energy dispersive X-ray fluorescence analysis with a portable equipment. Applied Radiation and Isotopes 68, 525–528. https://doi.org/10.1016/j.apradiso.2009.09.005

Clark, B.C., Baird, A.K., Rose, H.J., Toulmin, P., Christian, R.P., Kelliher, W.C., Castro, A.J., Rowe, C.D., Keil, K., Huss, G.R., 1977. The Viking X Ray Fluorescence Experiment: Analytical methods and early results. J. Geophys. Res. 82, 4577–4594. https://doi.org/10.1029/JS082i028p04577

Clark, B.C., Baird, A.K., Rose, H.J., Toulmin, P., Keil, K., Castro, A.J., Kelliher, W.C., Rowe, C.D., Evans, P.H., 1976. Inorganic Analyses of Martian Surface Samples at the Viking Landing Sites. Science 194, 1283–1288. https://doi.org/10.1126/science.194.4271.1283

Czyzycki, M., Wegrzynek, D., Wrobel, P., Lankosz, M., 2011. Monte Carlo simulation code for confocal 3D micro-beam X-ray fluorescence analysis of stratified materials. X-Ray Spectrom. 40, 88–95. https://doi.org/10.1002/xrs.1300

Dehouck, E., Gaudin, A., Chevrier, V., Mangold, N., 2016. Mineralogical record of the redox conditions on early Mars. Icarus 271, 67–75. https://doi.org/10.1016/j.icarus.2016.01.030

Domagal-Goldman, S.D., Wright, K.E., Adamala, K., Arina de la Rubia, L., Bond, J., Dartnell, L.R., Goldman, A.D., Lynch, K., Naud, M.-E., Paulino-Lima, I.G., Singer, K., Walter-

Antonio, M., Abrevaya, X.C., Anderson, R., Arney, G., Atri, D., Azúa-Bustos, A., Bowman, J.S., Brazelton, W.J., Brennecka, G.A., Carns, R., Chopra, A., Colangelo-Lillis, J., Crockett, C.J., DeMarines, J., Frank, E.A., Frantz, C., de la Fuente, E., Galante, D., Glass, J., Gleeson, D., Glein, C.R., Goldblatt, C., Horak, R., Horodyskyj, L., Kaçar, B., Kereszturi, A., Knowles, E., Mayeur, P., McGlynn, S., Miguel, Y., Montgomery, M., Neish, C., Noack, L., Rugheimer, S., Stüeken, E.E., Tamez-Hidalgo, P., Walker, S.I., Wong, T., 2016. The Astrobiology Primer v2.0. Astrobiology 16, 561–653. https://doi.org/10.1089/ast.2015.1460

dos Santos, R., Patel, M., Cuadros, J., Martins, Z., 2016. Influence of mineralogy on the preservation of amino acids under simulated Mars conditions. Icarus 277, 342–353. https://doi.org/10.1016/j.icarus.2016.05.029

Duvauchelle, P., Peix, G., Babot, D., 1999. Effective atomic number in the Rayleigh to Compton scattering ratio. Nuclear Instruments and Methods in Physics Research Section B: Beam Interactions with Materials and Atoms 155, 221–228.

Ebel, H., 1999. X-ray tube spectra. X-Ray Spectrometry 28, 255–266. https://doi.org/10.1002/(SICI)1097-4539(199907/08)28:4<255::AID-XRS347>3.0.CO;2-Y

Elam, W.T., Ravel, B.D., Sieber, J.R., 2002. A new atomic database for X-ray spectroscopic calculations. Radiation Physics and Chemistry 63, 121–128.

Elam, W.T., Shen, B., Scruggs, B., Nicolosi, J., 2006. Full spectrum calculations of EDXRF spectra. Powder diffraction 21, 152–155.

Flannigan, E.L., Campbell, J.L., 2017. Emulation of the Curiosity rover alpha particle X-ray spectrometer with accelerator-based PIXE: Implications for calibration. Nuclear

Instruments and Methods in Physics Research Section B: Beam Interactions with Materials and Atoms 413, 19–26. https://doi.org/10.1016/j.nimb.2017.10.002

Fleischer, M., 1969. U.S. Geological survey standards—I. Additional data on rocks G-1 and W-1, 1965–1967. Geochimica et Cosmochimica Acta 33, 65–79. https://doi.org/10.1016/0016-7037(69)90093-3

Gaillard, F., Scaillet, B., 2009. The sulfur content of volcanic gases on Mars. Earth and Planetary Science Letters 279, 34–43. https://doi.org/10.1016/j.epsl.2008.12.028

Gardner, R.P., Doster, J.M., 1978. The Reduction of Matrix Effects in X-Ray Fluorescence Analysis by the Monte Carlo, Fundamental Parameters Method. Adv. x-ray anal. 22, 343–356. https://doi.org/10.1154/S0376030800016712

Gellert, R., Rieder, R., Brückner, J., Clark, B.C., Dreibus, G., Klingelhöfer, G., Lugmair, G., Ming, D.W., Wänke, H., Yen, A., Zipfel, J., Squyres, S.W., 2006. Alpha Particle X-Ray Spectrometer (APXS): Results from Gusev crater and calibration report: APXS RESULTS FROM GUSEV CRATER. Journal of Geophysical Research: Planets 111. https://doi.org/10.1029/2005JE002555

Gellert, R., Yen, A.S., 2019. Elemental Analyses of Mars from Rovers Using the Alpha-Particle X-Ray Spectrometer, in: Bishop, J.L., Bell III, J.F., Moersch, J.E. (Eds.), Remote Compositional Analysis. Cambridge University Press, pp. 555–572. https://doi.org/10.1017/9781316888872.030

Ghidotti, M., Papoci, S., Dumitrascu, C., Zdiniakova, T., Fiamegos, Y., Gutiñas, M.B. de la C., 2021. ED-XRF as screening tool to help customs laboratories in their fight against fraud. State-of-the-art. Talanta Open 3, 100040. https://doi.org/10.1016/j.talo.2021.100040

Goudge, T.A., Mustard, J.F., Head, J.W., Fassett, C.I., Wiseman, S.M., 2015. Assessing the mineralogy of the watershed and fan deposits of the Jezero crater paleolake system, Mars: Jezero Paleolake System Mineralogy. Journal of Geophysical Research: Planets 120, 775–808. https://doi.org/10.1002/2014JE004782

Halevy, I., Zuber, M.T., Schrag, D.P., 2007. A Sulfur Dioxide Climate Feedback on Early Mars. Science 318, 1903–1907. https://doi.org/10.1126/science.1147039

Heirwegh, C.M., Campbell, J.L., Czamanske, G.K., 2016. Refinement of major- and minor-element PIXE analysis of rocks and minerals. Nuclear Instruments and Methods in Physics Research Section B: Beam Interactions with Materials and Atoms 366, 40–50. https://doi.org/10.1016/j.nimb.2015.10.018

Hodoroaba, V.-D., Rackwitz, V., 2014. Gaining Improved Chemical Composition by Exploitation of Compton-to-Rayleigh Intensity Ratio in XRF Analysis. Anal. Chem. 86, 6858–6864. https://doi.org/10.1021/ac5000619

Hodoroaba, V.-D., Radtke, M., Vincze, L., Rackwitz, V., Reuter, D., 2010. X-ray scattering in X-ray fluorescence spectra with X-ray tube excitation – Modelling, experiment, and Monte-Carlo simulation. Nuclear Instruments and Methods in Physics Research Section B: Beam Interactions with Materials and Atoms 268, 3568–3575. https://doi.org/10.1016/j.nimb.2010.09.017

Hofmann, B.A., 1990. Reduction spheroids from northern Switzerland: Mineralogy, geochemistry and genetic models. Chemical Geology 81, 55–81. https://doi.org/10.1016/0009-2541(90)90039-A

Horgan, B.H.N., Anderson, R.B., Dromart, G., Amador, E.S., Rice, M.S., 2020. The mineral diversity of Jezero crater: Evidence for possible lacustrine carbonates on Mars. Icarus 339, 113526. https://doi.org/10.1016/j.icarus.2019.113526

Jaffe, F., 1962. Oil Shale Part II: geology and mineralogy of the oil shales of the Green River formation, Colorado, Utah, Wyoming. Colorado School of Mines Mineral Industries Bulletin 5, 1–16.

Johansson, S.A.E., 1989. PIXE: a novel technique for elemental analysis. Endeavour 13, 48–53. https://doi.org/10.1016/0160-9327(89)90002-1

King, P.L., McLennan, S.M., 2010. Sulfur on Mars. Elements 6, 107–112. https://doi.org/10.2113/gselements.6.2.107

Kunzendorf, H., 1972. Quick determination of the average atomic number by X-ray scattering. Nuclear Instruments and Methods 99, 611–612. https://doi.org/10.1016/0029-554X(72)90676-3

Kurudirek, M., Büyükyıldız, M., 2016. Estimation of effective atomic number in the Rayleigh to Compton scattering ratio using different methods. Nuclear Instruments and Methods in Physics Research Section A: Accelerators, Spectrometers, Detectors and Associated Equipment 820, 80–84. https://doi.org/10.1016/j.nima.2016.03.029

Lanza, N.L., Wiens, R.C., Clegg, S.M., Ollila, A.M., Humphries, S.D., Newsom, H.E., Barefield, J.E., 2010. Calibrating the ChemCam laser-induced breakdown spectroscopy instrument for carbonate minerals on Mars. Applied Optics 49, C211. https://doi.org/10.1364/AO.49.00C211

Limaye, S.S., Mogul, R., Smith, D.J., Ansari, A.H., Słowik, G.P., Vaishampayan, P., 2018. Venus' Spectral Signatures and the Potential for Life in the Clouds. Astrobiology 18, 1181–1198. https://doi.org/10.1089/ast.2017.1783

Löwemark, L., Bloemsma, M., Croudace, I., Daly, J.S., Edwards, R.J., Francus, P., Galloway, J.M., Gregory, B.R.B., Steven Huang, J.-J., Jones, A.F., Kylander, M., Löwemark, L., Luo, Y., Maclachlan, S., Ohlendorf, C., Patterson, R.T., Pearce, C., Profe, J., Reinhardt, E.G., Stranne, C., Tjallingii, R., Turner, J.N., 2019. Practical guidelines and recent advances in the Itrax XRF core-scanning procedure. Quaternary International 514, 16–29. https://doi.org/10.1016/j.quaint.2018.10.044

Lynch, J., 1999. Additional Provisional Elemental Values for LKSD-1, LKSD-2, LKSD-3, LKSD-4, STSD-1, STSD-2, STSD-3 and STSD-4. Geostandards and Geoanalytical Research 23, 251–260. https://doi.org/10.1111/j.1751-908X.1999.tb00577.x

Lynch, J., 1990. Provisional Elemental Values for Eight New Geochemical Lake Sediment and Stream Sediment Reference Materials LKSD-1, LKSD-2, LKSD-3, LKSD-4, STSD-1, STSD-2, STSD-3 and STSD-4*. Geostandards and Geoanalytical Research 14, 153–167. https://doi.org/10.1111/j.1751-908X.1990.tb00070.x

Manninen, S., Koikkalainen, S., 1984. Determination of the effective atomic number using elastic and inelastic scattering of gamma rays. Int. J. Appl. Rad. Isot. 35, 965–968.

Manninen, S., Pitkänen, T., Koikkalainen, S., Paakkari, T., 1984. Study of the ratio of elastic to inelastic scattering of photons. The International Journal of Applied Radiation and Isotopes 35, 93–98. https://doi.org/10.1016/0020-708X(84)90190-X

Manso, M., Simão, R., Arruda, L., Carvalho, M.L., Pereira, F.A.B., 2019. Non-destructive X-ray fluorescence and Raman micro-analytical study of coffee drawings by Lagoa Henriques. Radiation Physics and Chemistry. https://doi.org/10.1016/j.radphyschem.2019.04.051

Mantler, M., Klikovits, J., 2004. Analysis of art objects and other delicate samples: Is XRF really nondestructive? Powder Diffr. 19, 16–19. https://doi.org/10.1154/1.1649962

Mantler, M., Schreiner, M., 2001. X-ray analysis of objects of art and archaeology. Journal of Radioanalytical and Nuclear Chemistry 247, 635–644.

Martindale Johnson, L.R., Ferguson, J.R., Freund, K.P., Drake, L., Duke, D., 2021. Evaluating obsidian calibration sets with portable X-Ray fluorescence (ED-XRF) instruments. Journal of Archaeological Science: Reports 39, 103126. https://doi.org/10.1016/j.jasrep.2021.103126

McCanta, M.C., Dyar, M.D., Dobosh, P.A., 2017. Extracting Bulk Rock Properties from Microscale Measurements: Subsampling and Analytical Guidelines. GSA Today 4–9. https://doi.org/10.1130/GSATG290A.1

McSween, H.Y., McGlynn, I.O., Rogers, A.D., 2010. Determining the modal mineralogy of Martian soils. J. Geophys. Res. 115, E00F12. https://doi.org/10.1029/2010JE003582

Michel-Hart, N., Elam, W.T., 2017. Low-energy shelf response in thin X-ray detectors from Compton scattering of hard X-rays.pdf. Nuclear Instruments and Methods in Physics Research Section A: Accelerators, Spectrometers, Detectors and Associated Equipment 863, 1–6. https://doi.org/10.1016/j.nima.2017.04.039

Mikhailov, I.F., Baturin, A.A., Mikhailov, A.I., Borisova, S.S., Surovitskiy, S.V., 2019. Dependence of the Compton to Rayleigh intensity ratio on the scatterer atomic number in the range of 4(Be) to 31(Ga). X-Ray Spectrometry. https://doi.org/10.1002/xrs.3117

Ming, D.W., Archer, P.D., Glavin, D.P., Eigenbrode, J.L., Franz, H.B., Sutter, B., Brunner, A.E., Stern, J.C., Freissinet, C., McAdam, A.C., Mahaffy, P.R., Cabane, M., Coll, P., Campbell, J.L., Atreya, S.K., Niles, P.B., Bell, J.F., Bish, D.L., Brinckerhoff, W.B., Buch, A., Conrad, P.G., Marais, D.J.D., Ehlmann, B.L., Fairén, A.G., Farley, K., Flesch, G.J., Francois, P., Gellert, R., Grant, J.A., Grotzinger, J.P., Gupta, S., Herkenhoff, K.E., Hurowitz, J.A., Leshin, L.A., Lewis, K.W., McLennan, S.M., Miller, K.E., Moersch, J., Morris, R.V., Navarro-González, R., Pavlov, A.A., Perrett, G.M., Pradler, I., Squyres, S.W., Summons, R.E., Steele, A., Stolper, E.M., Sumner, D.Y., Szopa, C., Teinturier, S., Trainer, M.G., Treiman, A.H., Vaniman, D.T., Vasavada, A.R., Webster, C.R., Wray, J.J., Yingst, R.A., Team, M.S., 2014. Volatile and Organic Compositions of Sedimentary Rocks in Yellowknife Bay, Gale Crater, Mars. Science 343, 1245267. https://doi.org/10.1126/science.1245267

Morris, R.V., Ruff, S.W., Gellert, R., Ming, D.W., Arvidson, R.E., Clark, B.C., Golden, D.C., Siebach, K., Klingelhöfer, G., Schröder, C., Fleischer, I., Yen, A.S., Squyres, S.W., 2010. Identification of Carbonate-Rich Outcrops on Mars by the Spirit Rover. Science 329, 421–424. https://doi.org/10.1126/science.1190545

Morris, R.V., Vaniman, D.T., Blake, D.F., Gellert, R., Chipera, S.J., Rampe, E.B., Ming, D.W., Morrison, S.M., Downs, R.T., Treiman, A.H., Yen, A.S., Grotzinger, J.P., Achilles, C.N., Bristow, T.F., Crisp, J.A., Marais, D.J.D., Farmer, J.D., Fendrich, K.V., Frydenvang, J., Graff, T.G., Morookian, J.-M., Stolper, E.M., Schwenzer, S.P., 2016. Silicic volcanism on Mars evidenced by tridymite in high-SiO2 sedimentary rock at Gale crater. PNAS 113, 7071–7076. https://doi.org/10.1073/pnas.1607098113

Mortazavi, M., Kavosh, H., Naghavi, S., Khanjari, R., 2022. Microstructural and Analytical Study of Uncommon Corrosion Features on Archaeological Cu-As Alloys from Tappeh Graziani in Southeastern Iran. Microscopy and Microanalysis. https://doi.org/10.1017/S1431927622000137

Mzyk, Z., Baranowska, I., Mzyk, J., 2002. Research on grain size effect in XRF analysis of pelletized samples. X-Ray Spectrometry 31, 39–46. https://doi.org/10.1002/xrs.534

Nielson, K.K., 1977. Matrix corrections for energy dispersive x-ray fluorescence analysis of environmental samples with coherent/incoherent scattered x-rays. Analytical chemistry 49, 641–648.

O'Connell-Cooper, C.D., Spray, J.G., Thompson, L.M., Gellert, R., Berger, J.A., Boyd, N.I., Desouza, E.D., Perrett, G.M., Schmidt, M., VanBommel, S.J., 2017. APXS-derived chemistry of the Bagnold dune sands: Comparisons with Gale Crater soils and the global Martian average: APXS-Bagnold Sands and Gale Soils. Journal of Geophysical Research: Planets 122, 2623–2643. https://doi.org/10.1002/2017JE005268

O'Connell-Cooper, C.D., Thompson, L.M., Spray, J.G., Berger, J.A., VanBommel, S.J., Gellert, R., Boyd, N.I., DeSouza, E., 2018. Chemical Diversity of Sands Within the Linear and Barchan Dunes of the Bagnold Dunes, Gale Crater, as Revealed by APXS Onboard Curiosity. Geophysical Research Letters 45, 9460–9470. https://doi.org/10.1029/2018GL079026

Olson, K.R., Straub, K.D., 2016. The Role of Hydrogen Sulfide in Evolution and the Evolution of Hydrogen Sulfide in Metabolism and Signaling. Physiology 31, 60–72. https://doi.org/10.1152/physiol.00024.2015

O'Neil, L.P., Catling, D.C., Elam, W.T., 2018. Optimized Compton fitting and modeling for light element determination in micro-X-ray fluorescence map datasets. Nuclear Instruments and Methods in Physics Research Section B: Beam Interactions with Materials and Atoms 436, 173–178. https://doi.org/10.1016/j.nimb.2018.09.023

Perrett, G.M., Campbell, J.L., Gellert, R., King, P.L., Nield, E., O'Meara, J.M., Pradler, I., 2016. Refinement of the Compton–Rayleigh scatter ratio method for use on the Mars Science Laboratory alpha particle X-ray spectrometer: II – Extraction of invisible element content. Nuclear Instruments and Methods in Physics Research Section B: Beam Interactions with Materials and Atoms 368, 129–137. https://doi.org/10.1016/j.nimb.2015.10.076

Pontefract, A., Zhu, T.F., Walker, V.K., Hepburn, H., Lui, C., Zuber, M.T., Ruvkun, G., Carr, C.E., 2017. Microbial Diversity in a Hypersaline Sulfate Lake: A Terrestrial Analog of Ancient Mars. Front. Microbiol. 8, 1819. https://doi.org/10.3389/fmicb.2017.01819

Rieder, R., Gellert, R., Brückner, J., Klingelhöfer, G., Dreibus, G., Yen, A., Squyres, S.W., 2003. The new Athena alpha particle X-ray spectrometer for the Mars Exploration Rovers: NEW APXS FOR MER. J.-Geophys.-Res. 108. https://doi.org/10.1029/2003JE002150

Rieder, R., Wänke, H., Economou, T., Turkevich, A., 1997. Determination of the chemical composition of Martian soil and rocks: The alpha proton X ray spectrometer. J. Geophys. Res. 102, 4027–4044. https://doi.org/10.1029/96JE03918

Rivera-Hernández, F., Sumner, D.Y., Mangold, N., Stack, K.M., Forni, O., Newsom, H., Williams, A., Nachon, M., L'Haridon, J., Gasnault, O., Wiens, R., Maurice, S., 2019. Using ChemCam LIBS data to constrain grain size in rocks on Mars: Proof of concept and application to rocks at Yellowknife Bay and Pahrump Hills, Gale crater. Icarus 321, 82–98. https://doi.org/10.1016/j.icarus.2018.10.023

Sadeghalvad, B., Khorshidi, N., Azadmehr, A., Sillanpää, M., 2021. Sorption, mechanism, and behavior of sulfate on various adsorbents: A critical review. Chemosphere 263, 128064. https://doi.org/10.1016/j.chemosphere.2020.128064

Santos, A., Filiberto, J., Ganesh, I., Gilmore, M., Lewis, J.A., Treiman, A.H., 2021. Venus Petrology: The Need for New Data. Bulletin of the AAS 53. https://doi.org/10.3847/25c2cfeb.c73e5040

Schiavon, N., de Palmas, A., Bulla, C., Piga, G., Brunetti, A., 2016. An Energy-Dispersive X-Ray Fluorescence Spectrometry and Monte Carlo simulation study of Iron-Age Nuragic small bronzes (“Navicelle”) from Sardinia, Italy. Spectrochimica Acta Part B: Atomic Spectroscopy 123, 42–46. https://doi.org/10.1016/j.sab.2016.07.011

Schoonjans, T., Brunetti, A., Golosio, B., Sanchez del Rio, M., Solé, V.A., Ferrero, C., Vincze, L., 2011. The xraylib library for X-ray–matter interactions. Recent developments. Spectrochimica Acta Part B: Atomic Spectroscopy 66, 776–784. https://doi.org/10.1016/j.sab.2011.09.011

Schoonjans, T., Vincze, L., Solé, V.A., Sanchez del Rio, M., Brondeel, P., Silversmit, G., Appel, K., Ferrero, C., 2012. A general Monte Carlo simulation of energy dispersive X-ray fluorescence spectrometers — Part 5: Polarized radiation, stratified samples, cascade effects, M-lines. Spectrochimica Acta Part B: Atomic Spectroscopy 70, 10–23. https://doi.org/10.1016/j.sab.2012.03.011

Sholes, S.F., Smith, M.L., Claire, M.W., Zahnle, K.J., Catling, D.C., 2017. Anoxic atmospheres on Mars driven by volcanism: Implications for past environments and life. Icarus 290, 46–62. https://doi.org/10.1016/j.icarus.2017.02.022

Smith, M.L., Claire, M.W., Catling, D.C., Zahnle, K.J., 2014. The formation of sulfate, nitrate and perchlorate salts in the martian atmosphere. Icarus 231, 51–64. https://doi.org/10.1016/j.icarus.2013.11.031

Spinks, S.C., Parnell, J., Bowden, S.A., 2010. Reduction spots in the Mesoproterozoic age: implications for life in the early terrestrial record. International Journal of Astrobiology 9, 209–216. https://doi.org/10.1017/S1473550410000273

Sprang, H. van, Bekkers, M.H.J., 1998. Determination of light elements using x-ray spectrometry. Part I—Analytical implications of using scattered tube lines. X-Ray Spectrometry 27, 31–36. https://doi.org/10.1002/(SICI)1097-4539(199801/02)27:1<31::AID-XRS245>3.0.CO;2-#

Squyres, S.W., Arvidson, R.E., Bell, J.F., Brückner, J., Cabrol, N.A., Calvin, W., Carr, M.H., Christensen, P.R., Clark, B.C., Crumpler, L., Marais, D.J.D., d'Uston, C., Economou, T., Farmer, J., Farrand, W., Folkner, W., Golombek, M., Gorevan, S., Grant, J.A., Greeley, R., Grotzinger, J., Haskin, L., Herkenhoff, K.E., Hviid, S., Johnson, J., Klingelhöfer, G., Knoll, A.H., Landis, G., Lemmon, M., Li, R., Madsen, M.B., Malin, M.C., McLennan, S.M., McSween, H.Y., Ming, D.W., Moersch, J., Morris, R.V., Parker, T., Rice, J.W., Richter, L., Rieder, R., Sims, M., Smith, M., Smith, P., Soderblom, L.A., Sullivan, R., Wänke, H., Wdowiak, T., Wolff, M., Yen, A., 2004. The Opportunity Rover's Athena Science Investigation at Meridiani Planum, Mars. Science 306, 1698–1703. https://doi.org/10.1126/science.1106171

Squyres, S.W., Arvidson, R.E., Ruff, S., Gellert, R., Morris, R.V., Ming, D.W., Crumpler, L., Farmer, J.D., Marais, D.J.D., Yen, A., McLennan, S.M., Calvin, W., Bell, J.F., Clark, B.C., Wang, A., McCoy, T.J., Schmidt, M.E., Souza, P.A. de, 2008. Detection of Silica-Rich Deposits on Mars. Science 320, 1063–1067. https://doi.org/10.1126/science.1155429

Surkov, Yu.A., Barsukov, V.L., Moskalyeva, L.P., Kharyukova, V.P., Kemurdzhian, A.L., 1984. New data on the composition, structure, and properties of Venus rock obtained by Venera 13 and Venera 14. J. Geophys. Res. 89, B393. https://doi.org/10.1029/JB089iS02p0B393

Terashima, S., Imai, N., Taniguchi, M., Okai, T., Nishimura, A., 2002. The Preparation and Preliminary Characterisation of Four New Geological Survey of Japan Geochemical Reference Materials: Soils, JSO-1 and JSO-2; and Marine Sediments, JMS-1 and JMS-2. Geostandards and Geoanalytical Research 26, 85–94. https://doi.org/10.1111/j.1751-908X.2002.tb00626.x

Tertian, R., Claisse, F., 1982. Principles of quantitative X-ray fluorescence analysis. Heyden, London, UK.

Thompson, D.R., Flannery, D.T., Lanka, R., Allwood, A.C., Bue, B.D., Clark, B.C., Elam, W.T., Estlin, T.A., Hodyss, R.P., Hurowitz, J.A., Liu, Y., Wade, L.A., 2015. Automating X-ray Fluorescence Analysis for Rapid Astrobiology Surveys. Astrobiology 15, 961–976. https://doi.org/10.1089/ast.2015.1349

Thompson, L.M., Schmidt, M.E., Spray, J.G., Berger, J.A., Fairén, A.G., Campbell, J.L., Perrett, G.M., Boyd, N., Gellert, R., Pradler, I., VanBommel, S.J., 2016. Potassium-rich sandstones within the Gale impact crater, Mars: The APXS perspective: Potassium-Rich Sandstones on Mars. Journal of Geophysical Research: Planets 121, 1981–2003. https://doi.org/10.1002/2016JE005055

Tian, F., Claire, M.W., Haqq-Misra, J.D., Smith, M., Crisp, D.C., Catling, D., Zahnle, K., Kasting, J.F., 2010. Photochemical and climate consequences of sulfur outgassing on early Mars.

Earth and Planetary Science Letters 295, 412–418. https://doi.org/10.1016/j.epsl.2010.04.016

Tian, S., Lu, L., Labavitch, J.M., Webb, S.M., Yang, X., Brown, P.H., He, Z., 2014. Spatial imaging of Zn and other elements in Huanglongbing-affected grapefruit by synchrotron-based micro X-ray fluorescence investigation. J. Exp. Bot. 65, 953–964. https://doi.org/10.1093/jxb/ert450

Usui, T., Righter, K., Shearer, C.K., Jones, John H., 2022. Effect of sulfur on siderophile element partitioning between olivine and a primary melt from the martian mantle. American Minerologist 107, 357–368.

Van Espen, P., 2002. Spectrum Evaluation, in: R. van (René) Grieken, Markowicz, A. (Eds.), Handbook of X-Ray Spectrometry, Practical Spectroscopy. Marcel Dekker, New York.

van Espen, P., Nullens, H., Adams, F., 1977. A computer analysis of X-ray fluorescence spectra. Nuclear Instruments and Methods 142, 243–250. https://doi.org/10.1016/0029-554X(77)90834-5

van Grieken, R., Markowicz, A. (Eds.), 2002. Handbook of X-ray Spectrometry, 2nd ed., rev.expanded. ed, Practical spectroscopy ; v. 29. Marcel Dekker, New York.

Van Gysel, M., Lemberge, P., Van Espen, P., 2003. Description of Compton peaks in energy-dispersive x-ray fluorescence spectra. X-Ray Spectrometry 32, 139–147. https://doi.org/10.1002/xrs.628

Vaniman, D.T., Bish, D.L., Chipera, S.J., Fialips, C.I., William Carey, J., Feldman, W.C., 2004. Magnesium sulphate salts and the history of water on Mars. Nature 431, 663–665. https://doi.org/10.1038/nature02973

Vincze, L., Janssens, K., Adams, F., 1993. A General Monte-Carlo Simulation of Energy-Dispersive X-ray-Fluorescence Spectrometers Part 1. Unpolarized Radiation, Homogeneous Samples. Spectrochimica Acta Part B 48, 553–573.

Vincze, L., Janssens, K., Adams, F., Rivers, M.L., Jones, K.W., 1995. A general Monte Carlo simulation of ED-XRF spectrometers. II: Polarized monochromatic radiation, homogeneous samples. Spectrochimica Acta Part B: Atomic Spectroscopy 50, 127–147. https://doi.org/10.1016/0584-8547(94)00124-E

Vine, J.D., Tourtelot, E.B., 1969. Geochemical investigations of some black shales and associated rocks (USGS Bulletin No. 1314- A). https://doi.org/10.3133/b1314A

Westall, F., Foucher, F., Bost, N., Bertrand, M., Loizeau, D., Vago, J.L., Kminek, G., Gaboyer, F., Campbell, K.A., Bréhéret, J.-G., Gautret, P., Cockell, C.S., 2015. Biosignatures on Mars: What, Where, and How? Implications for the Search for Martian Life. Astrobiology 15, 998–1029. https://doi.org/10.1089/ast.2015.1374

Wiens, R.C., Maurice, S., Perez, F.R., 2017. The SuperCam Remote Sensing Instrument Suite for the Mars 2020 Rover: A Preview. Spectroscopy 32, 50–55.

Williford, K.H., Farley, K.A., Stack, K.M., Allwood, A.C., Beaty, D., Beegle, L.W., Bhartia, R., Brown, A.J., de la Torre Juarez, M., Hamran, S.-E., Hecht, M.H., Hurowitz, J.A., Rodriguez-Manfredi, J.A., Maurice, S., Milkovich, S., Wiens, R.C., 2018. The NASA Mars 2020 Rover Mission and the Search for Extraterrestrial Life, in: Cabrol, N.A., Grin, E.A. (Eds.), From Habitability to Life on Mars. Elsevier, pp. 275–308. https://doi.org/10.1016/B978-0-12-809935-3.00010-4

Yen, A.S., Gellert, R., Schröder, C., Morris, R.V., Bell, J.F., Knudson, A.T., Clark, B.C., Ming, D.W., Crisp, J.A., Arvidson, R.E., Blaney, D., Brückner, J., Christensen, P.R., DesMarais, D.J., de Souza, P.A., Economou, T.E., Ghosh, A., Hahn, B.C., Herkenhoff, K.E., Haskin, L.A., Hurowitz, J.A., Joliff, B.L., Johnson, J.R., Klingelhöfer, G., Madsen, M.B., McLennan, S.M., McSween, H.Y., Richter, L., Rieder, R., Rodionov, D., Soderblom, L., Squyres, S.W., Tosca, N.J., Wang, A., Wyatt, M., Zipfel, J., 2005. An integrated view of the chemistry and mineralogy of martian soils. Nature 436, 49–54. https://doi.org/10.1038/nature03637

Yi, L., Liu, Z., Wang, K., Chen, M., Peng, S., Zhao, W., He, J., Zhao, G., 2015. A new background subtraction method for energy dispersive X-ray fluorescence spectra using a cubic spline interpolation. Nuclear Instruments and Methods in Physics Research Section A: Accelerators, Spectrometers, Detectors and Associated Equipment 775, 12–14. https://doi.org/10.1016/j.nima.2014.11.100

Zheng, L.-N., Ma, R.-L., Li, Q., Sang, Y.-B., Wang, H.-L., Wang, B., Yan, Q.-Q., Chen, D.-L., Wang, M., Feng, W.-Y., Zhao, Y.-L., 2019. Elemental analysis and imaging of sunscreen fingermarks by X-ray fluorescence. Analytical and Bioanalytical Chemistry. https://doi.org/10.1007/s00216-019-01718-0